J. Fluid Mech. (1987), *vol.* 178, *pp.* 1–29
Printed in Great Britain

Energy separation in a vortex street

By M. KUROSAKA[†], J. B. GERTZ[‡],
Massachusetts Institute of Technology, Cambridge, MA 02139, USA

J. E. GRAHAM,
Air Force Wright Aeronautical Laboratories, Wright Patterson Air Force Base,
OH 45433, USA

J. R. GOODMAN, P. SUNDARAM, W. C. RINER[§],
H. KURODA[‖]
The University of Tennessee Space Institute, Tullahoma, TN 37388, USA

AND W. L. HANKEY
The Wright State University, Dayton, OH 45433, USA

(Received 2 January 1986 and in revised form 17 July 1986)

When a bluff body is placed in a crossflow, the total temperature in its wake can become substantially less than the incoming one, as manifested by the fact that the recovery factor R on its rearmost surface takes negative values at high subsonic flow: this is the phenomenon referred to here as the Eckert–Weise effect. Although a vortex street has been a suspected cause, the issue of whether this is so, and what the mechanism is, has remained unsettled. In this experimental and theoretical investigation, we first examine the cause of the Eckert–Weise effect by enhancing the vortex shedding through acoustic synchronization: resonance between the vortex shedding and transversely standing acoustic waves in a wind tunnel. At the lowest synchronization, where a ringing sound emanates from the wind tunnel, R at the rearmost section of the cylinder is found to become negative even at a Mach number of 0.2; the base pressure (C_{pb}) takes dips correspondingly, indicative of the intensification of the vortex street. At this lowest acoustic resonance, the decrease of R and C_{pb}, uniform along the span, agrees with the expectation based on the spanwise uniformity of the lowest standing wave. At the next acoustic resonance where the standing wave now varies along the span, the corresponding dips in R and C_{pb}, non-uniform along the span, reveals an interesting 'strip-theory'-like behaviour of the vortex intensities in the vortex street. These results correlating the change in R with C_{pb} confirm that the Eckert–Weise effect is indeed caused by the vortex shedding, the mechanism of which is examined theoretically in the latter half of the paper.

A simple theoretical argument, bolstered by a full numerical simulation, shows that the time-varying static pressure field due to the vortex movement separates the instantaneous total temperature into hot and cold spots located around vortices; once time-averaged, however, the total temperature distribution conceals the presence of hot spots and takes the guise of a colder wake, the Eckert–Weise effect. Therefore the correct explanation of the Eckert–Weise effect, a time-averaged phenomenon,

---

[†] Present address: The University of Tennessee Space Institute, Tullahoma, Tennessee 37388.
[‡] Present address: Pratt & Whitney Aircraft, Hartford, Connecticut 06108.
[§] Present address: Teledyne Brown Engineering, Huntsville, Alabama 35807.
[‖] Present address: Japan Defense Academy, Yokosuka, Japan.

emerges only out of, and only as a superposition of, instantaneous total temperature separation around vortices. Such a separation is not confined to the outside of vortex cores; every vortex in its entirety becomes thermally separated. Nor is it limited to the far downstream equilibrium configuration of the Kármán vortex street but applies to the important near-wake vortices, and to any three-dimensional vortical structure as well. For low subsonic flows in particular, this dynamical explanation also leads to a similar separation of total pressure; these features may thus be potentially exploited as a general marker to identify and quantify vortices.

1. Introduction

In a recent article, Eckert (1984) rekindled general interest in a curious but still unresolved phenomenon, the cooling effect in the wake behind a cylinder. In 1943, he and Weise, while measuring the surface temperature around a thermally insulated cylinder placed in air, had found this (Eckert & Weise 1943): for the cylinder in a crossflow, although the surface temperature at the forward stagnation point attained its expected upstream stagnation value, at the rearmost point the surface temperature was found to drop by as much as 20 °C, to the extent that it was even lower than the upstream static temperature. In terms of the recovery factor defined as $(T(\theta)-T_\infty)/(T_{t\infty}-T_\infty)$ (where $T(\theta)$ is the surface or total temperature at an angular position θ measured from the forward stagnation point, T_∞ the upstream static temperature and $T_{t\infty}$ the upstream total temperature), while at the forward stagnation point ($\theta = 0°$) the recovery factor is equal to 1, at the rearmost point ($\theta = 180°$) it becomes *negative*, equal to about -0.1 at a free-stream Mach number of 0.65. This finding, hereafter called the Eckert–Weise effect, is in marked contrast to the well-known, much higher values of the recovery factor for the boundary layer over a flat plate: 0.84 for a laminar one, 0.90 for turbulent.

The Eckert–Weise effect, which surprised Prandtl of all people, was later confirmed by Ryan (1951). Even for bluff bodies other than a cylinder he found the presence of lowered temperature, which is not limited to the surface of bodies but extends to the downstream wake as well. In addition, he narrated a particularly arresting observation: at the Mach number of about 0.7, he suddenly heard a whistling noise and at that instant he noticed a drop in the recovery factor. Although it led him to presume that a certain form of tunnel resonance was involved, this speculation was not pursued further. As the general cause of the Eckert–Weise effect, Ryan also postulated that vortex streets shed by bluff bodies might somehow be responsible; this supposition later led to the potential-flow theory applied to the wake pioneered by Ackeret (1954), which in turn was adversely criticized by Schultz-Grunow (1960). For a reason to become self-evident, their discussion is relegated to the latter half of the paper, where the mechanism of the phenomenon is discussed.

The data of Eckert & Weise and Ryan were all taken by thermocouples, which can, of course, measure only the time-averaged values. Thus, to be precise, the Eckert–Weise effect should refer, as will be done hereafter, to the defect in time-averaged surface temperature or total temperature in the flow.

Besides these experimental data, the cooling effect is also manifest in our recent result of a numerically computed flow behind a body: the colour graphic of figure 1 (*a*) (Plate 1) (its numerical scheme will be discussed in §10) displays the time-averaged total temperature distribution calculated around a stationary, thermally insulated

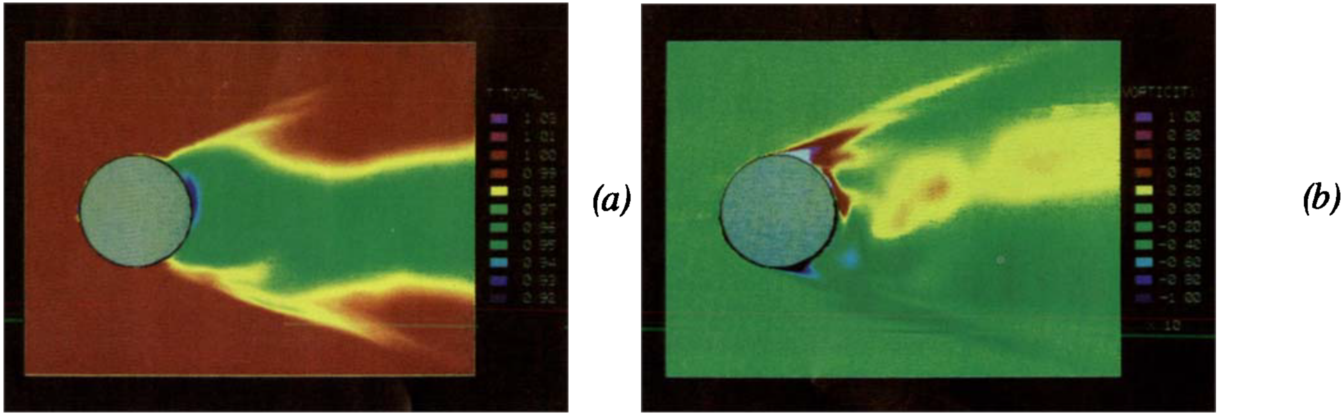

FIGURE 1. Time-averaged total temperature (*a*) and vorticity (*b*) distributions computed by large-scale structure simulation. The upstream flow on the far left is uniform; the cylinder is stationary, its surface thermally insulated: T_t is non-dimensionalized by $T_{t\infty}$; vorticity by U_∞ and *d*; $M_\infty = 0.35$, $Re = 1.4 \times 10^5$.

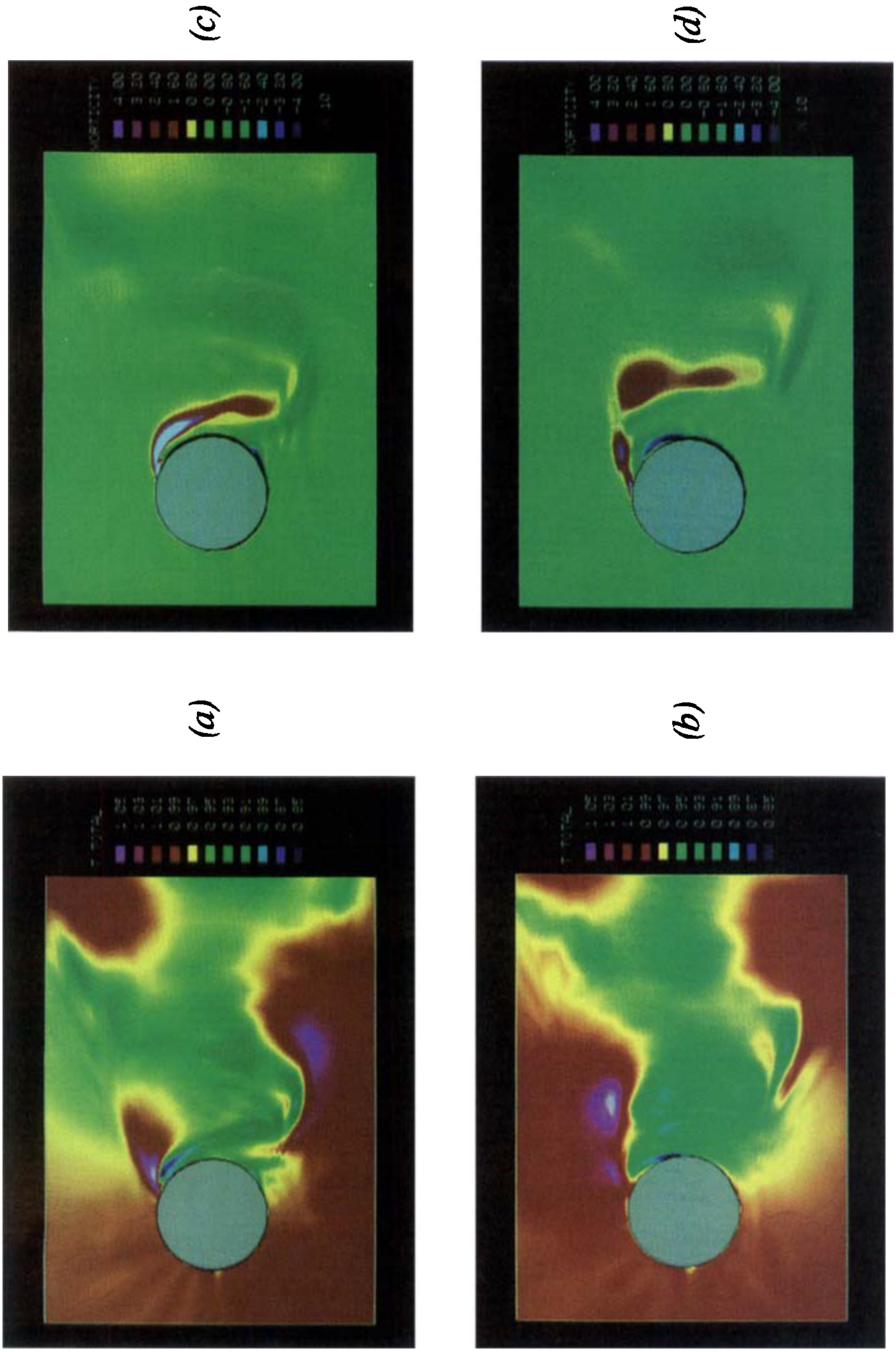

FIGURE 10. Instantaneous total temperature (*a*, *b*) and vorticity (*c*, *d*) distributions computed by large-scale structure simulation. For description, see figure 1; note the difference of colour grades between figures 1 and 10.

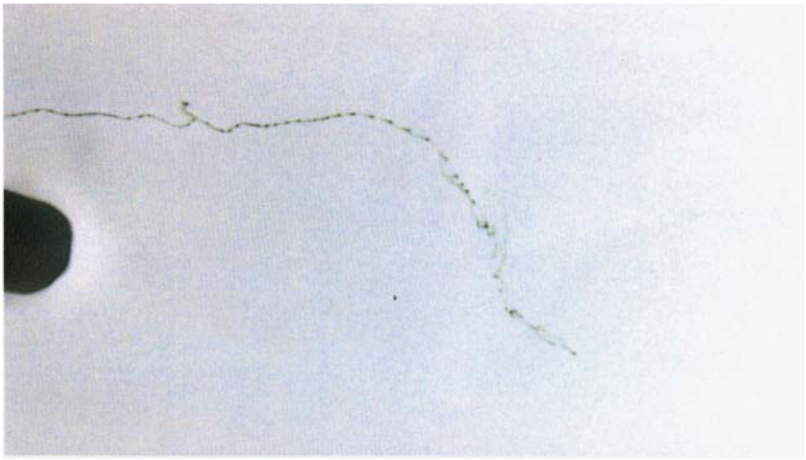

(*a*)

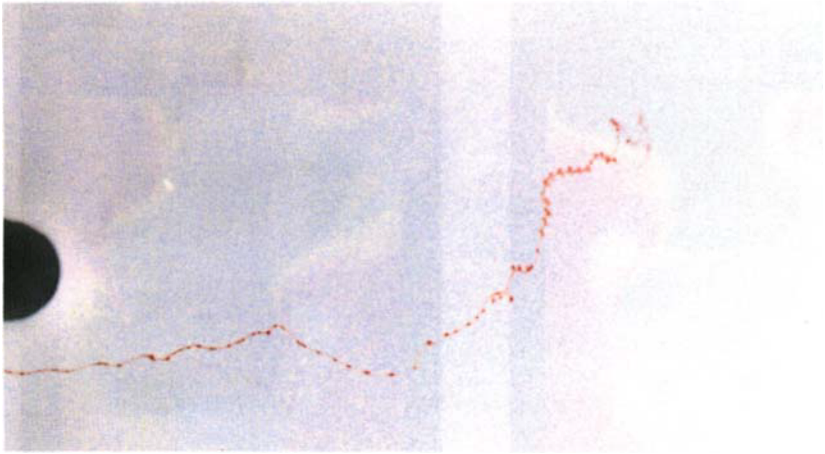

(*b*)

FIGURE 14. Dyelines crossing over the wake in water. Flow is from left to right; (*a*) viewed from the downstream, the green dye is initially injected on the right side of the upstream flow field; (*b*) the red dye is injected on the left side: $d = 3.2$ cm; $U_{\infty} = 8.9$ cm/s, $Re = 2.3 \times 10^3$ and the width of the test section is 20.3 cm.

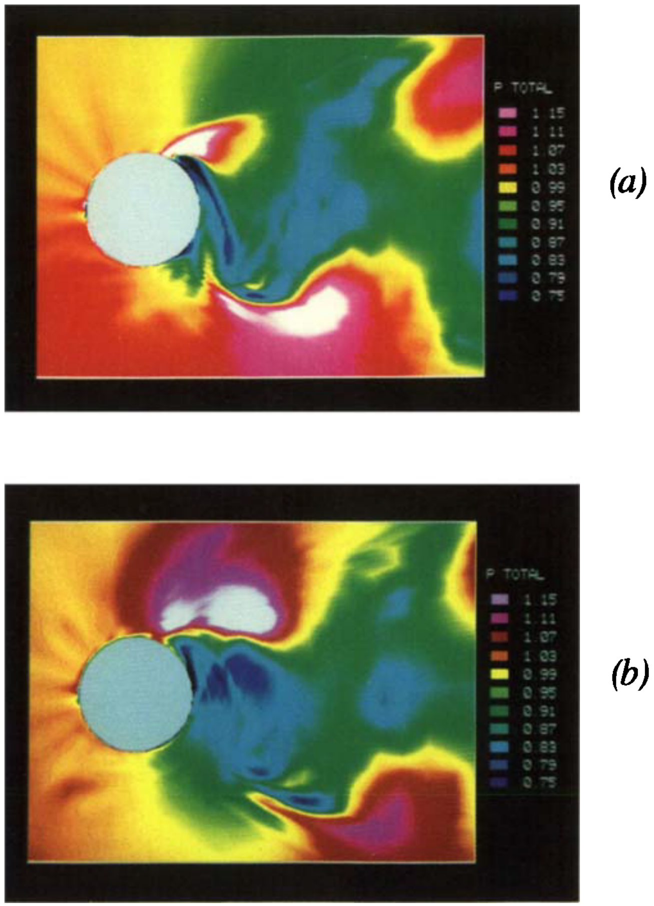

FIGURE 15. Instantaneous total pressure distribution computed by large-scale structure simulation: (*a*) corresponds to figure 10(*a*), (*b*) to 10(*b*); P_t is normalized by $P_{t\infty}$.

cylinder immersed in uniform flow, at a free-stream Mach number of 0.35 and a Reynolds number 1.4×10^5. Notice that the coldest spot around the cylinder periphery is at the rearward section and a traverse in the vertical y-direction would show the presence of the coldest spot at the wake centreline; despite a slight degree of numerical asymmetry, these are all in qualitative agreement with the experimental data.

After Ryan, Thomann (1959) showed that the attachment of a splitter plate behind a wedge raises the recovery factor around its rearmost point while suppressing the vortex street, the latter being an effect initially found by Roshko (1955). Although it may not be entirely unreasonable to assume from this that the vortex street could be an apparent cause of the cooling, the insertion of a physical object such as a splitter plate has an obvious drawback: at the junction between the body and the splitter plate, another stagnation point would be formed; this could conceivably raise the recovery factor around it. Thus not only the mechanism of the Eckert–Weise effect but even its cause, to a certain extent, has remained unresolved.

In the experiments discussed in the first half of this paper, instead of suppressing the vortex street shed from a cylinder, we *intensify* the vortex street by the use of a non-invasive means and test whether one could further lower the wake temperature. Such a demonstration, which does not involve any alteration to the body shape, could show that the vortex street is indeed the cause of the cooling effect.

As a non-intrusive means of excitation, we make use of wind-tunnel acoustic resonance: synchronization between the frequency of vortex shedding from a cylinder and that of transversely standing acoustic waves, the latter being latently present in any wind tunnel. In the normal operation of a wind tunnel, one avoids the condition of acoustic resonance but here we exploit it deliberately and fully. Although vibrating a cylinder could achieve the same goal, acoustic resonance, owing to its obvious simplicity realizable by the mere presence of wind-tunnel walls only – without any additional provision – offers a decisive advantage.

In fact, we found that acoustic resonance with a cylinder can cause transversely standing acoustic waves to materialize not only with ease but in form strikingly close to idealized normal modes; this occurs not only for the fundamental mode but also for higher modes (therefore in this regard wind-tunnel acoustic resonance appears to surpass other excitation methods such as synchronization by speakers).

This ability of acoustic resonance to reproduce with fidelity higher normal modes as well as the fundamental one has several advantages here, which are best described by referring to figure 4. Within the square cross-section of the wind tunnel surrounded by the top, bottom and sidewalls, the flow being perpendicular to the paper, the expected positions of loops and nodes for the y-component of acoustic velocity v', are shown schematically for the first three normal modes (since for the fundamental or lowest normal mode (*a*) and the third normal mode (*c*), it is difficult to draw the appropriate waveform corresponding to the vertical motion, arrows depicting the movement are drawn horizontally but they in fact represent the y-component of acoustic velocity). Waveforms are shown in the absence of the test cylinder, which would be normally placed along the z-axis; as the order of modes becomes higher, the corresponding acoustic frequencies increase.

If the cylinder is placed along the z-axis and when the vortex-shedding frequency, which increases proportionally to the flow velocity, approaches any of acoustic frequencies, we expect that the shedding frequency will become locked to the acoustic frequency and remain so over a certain range of Mach numbers. Thus, as the Mach number is progressively increased, the vortex-shedding process undergoes a sequence of locked-in regimes, the first lock-in corresponding to the lowest normal mode, the second lock-in to the next normal mode and so forth. Although at these lock-ins, the strength of the vortex street becomes, in general, intensified, its degree and details of local flow response may differ depending on the location of acoustic nodes and loops.

For instance, as indicated in figure 4(*a*), at the first lock-in the loop of the vertical acoustic velocity coincides with the cylinder position, the z-axis; hence the acoustic loop is located in the vicinity of vertically fluctuating fluid, induced by the vortex street. Thus here we expect strong resonance and so intensification of the vortex street. Furthermore, owing to the alignment of the loop and cylinder axis, such intensification is expected to manifest itself more or less uniformly along the span of the cylinder; if the vortex street indeed causes the Eckert–Weise effect, one may be able to demonstrate that the temperature behind the cylinder drops *uniformly along the span* for the first lock-in.

At the second lock-in, figure 4(*b*), where a node is located at the midspan and loops on the sidewalls, the vortex street might become intensified non-uniformly along the span. That is, if and when the strength of the vortex street differs from one point to another, varying along the span in direct response to locally varying stimuli, then we anticipate little change in the vortices at the midspan in contrast to stronger vortices at off-midspan points; again, if the Eckert–Weise effect in the wake is controlled by the vortex street, the temperture drop behind the cylinder may *vary along the span* accordingly for the second lock-in.

Figure 9(*e*), our central results, indeed fulfills these expectations. Thus in §4, the experimental part of the investigation, we conclude that vortex shedding is indeed the cause of the Eckert–Weise effect.

In investigating next how the vortex shedding causes the cooling effect, we turn to the time-varying, instantaneous flow field computed by the numerical code used for the time-averaged total temperature distribution of figure 1(*a*), since the calculated unsteady velocity field does reproduce the long-familiar characteristics of vortex shedding with Strouhal number around 0.2, an appropriate value for this Reynolds number.

When we look at such instantaneous snapshots of time-varying total temperature distributions as figures 10(*a*) and (*b*) (Plate 2) they, however, reveal unexpected features hidden in the average: the temporary existence of *hot spots*, with total temperature higher than that of the incoming flow (white spots correspond to the region with temperature higher than those in pink) as well as the expected presence of cold spots. And furthermore, *hot and cold spots exist seemingly side by side*. When a time sequence of instantaneous total temperature distributions such as figure 10(*b*), taken after figure 10(*a*), is successively superimposed, the result is figure 1(*a*); the deceptive time-averaged wake does not betray a hint of instantaneous hot spots.

A simple dynamical explanation for this is to be found in §5, other theoretical considerations following thereafter. Chief among them is the discussion of §7, where we point out that for low subsonic flows, the total pressures separate as well and their near-wake patterns, shown in figure 15 (Plate 4), are almost replicas of those of total temperatures, figure 10.

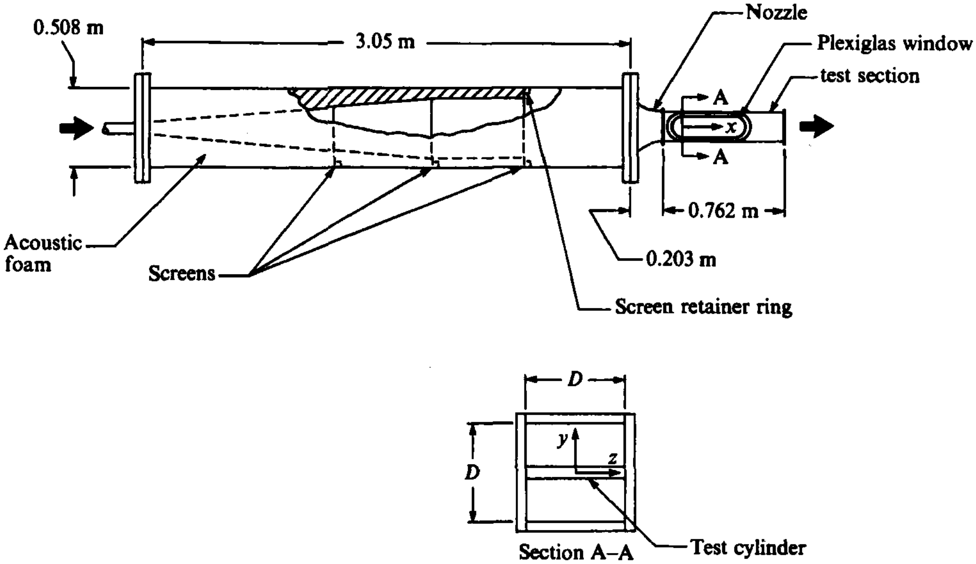

FIGURE 2. Test-rig layout; $D = 15.24$ cm.

2. Test apparatus

In order to achieve resonance between the vortex-shedding frequency and the natural frequency of standing acoustic waves in the wind tunnel, it is necessary to minimize any extraneous background noise. For this, a special, low-noise wind tunnel has been designed and built at the University of Tennessee Space Institute. As shown in figure 2, the interior of a settling tank (0.508 m in diameter and 3.050 m in length), to which compressed air is introduced first, is covered with specially formed acoustic foams: starting from the inlet, the internal surface of the acoustic foam is shaped as a diffuser. This provides an effective reduction of background noise such that in the test section the sound level at $M_\infty = 0.5$ (M_∞ is the free-stream Mach number in the test section) is less than 110 dB for frequency over 500 Hz. Three fine-meshed screens are installed in the settling tank to make the flow uniform.

The cross-section of the test section is a square, $D = 15.24$ cm; its size is chosen so that with a cylinder of 12.7 mm in diameter placed transverse to the flow the first lock-in can take place at a low subsonic Mach number, $M_\infty = 0.21$. This low Mach number was selected because past investigations on the Eckert–Weise effect behind the cylinder were all conducted with high subsonic to supersonic flow: $M_\infty = 0.65$ for Eckert & Weise, $M_\infty = 0.4$–0.7 for Ryan and $M_\infty = 0.56$–3 for Thomann. However, if a vortex street is the cause, the drop in wake temperature or negative recovery factor should occur even in this low subsonic flow.

Within the test section, the uniformity of velocity and temperature profiles outside the boundary layers is confirmed. Aft of the test section, the air discharges directly to the atmosphere.

To meet our objective of sustaining the temperature drop across the cylinder, thermally insulating material was needed; rods of Polyvinyl Chloride (PVC) and Acetal (Delrin) were selected in the preliminary tests. Since both materials were found to yield similar results, the main test is conducted with a PVC rod, 12.7 mm in diameter (d) and 15.24 cm in effective length, as shown in figure 3. To increase the thermal response of this thermally insulating material to the air temperature in the

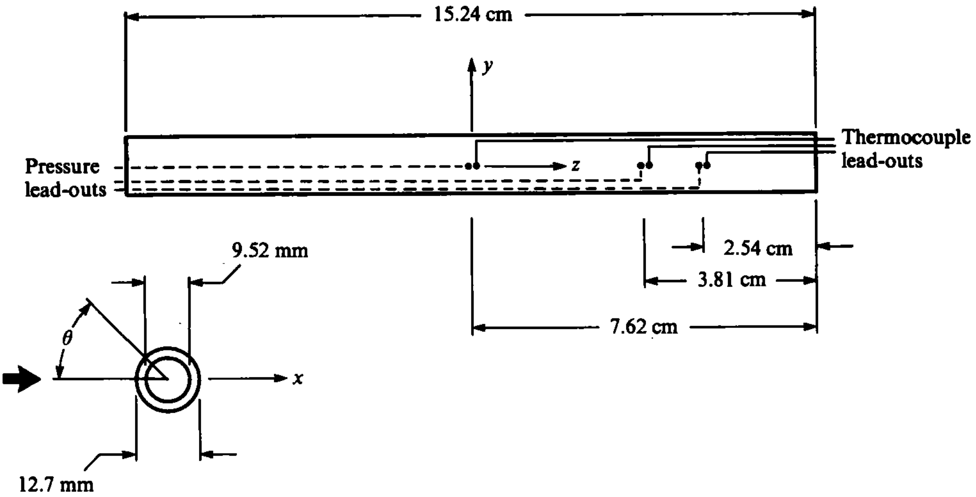

FIGURE 3. Test cylinder.

test section, the cylinder is hollow, the inner diameter of the drilled-out cavity being 9.52 mm, and this inner space is evacuated prior to each test in order to increase the effective thermal diffusivity of the rod by the reduction of air density. Thus, during the main part of a test run, which typically lasts about 20 minutes, quick thermal response and equilibrium are found to become established, even though the incoming temperature drops continually owing to the blow-down mode of operation.

The origin of the x-coordinate, aligned along the free-stream direction, is at the centre of the cylinder, the y- and z-coordinates, being, as shown in figure 3, perpendicular and parallel to the cylinder respectively.

The cylinder is instrumented with thermocouples and pressure taps. At $\theta = 0°$ or the forward stagnation point, three pairs of thermocouples and pressure taps are imbedded on the cylinder surface: (1) at the centre, (2) at a quarter-point and (3) 2.54 cm away from the wall. At $\theta = 180°$, the rearmost point, there were similarly three pairs of thermocouples and pressure taps. Thermocouples are of Chromel–Alumel type, 0.127 mm in diameter. The grooves to insert them are initially cut on the cylinder surface and later covered with fibreglass fillers so that cylinder surface remains smooth and circular.

Total temperature is monitored by a thermocouple installed within the settling tank, and the free-stream Mach number by a calibrated total and static pressure probe inserted in the test section and located upstream of the cylinder, at $x/d = -5.75$. The temperature scanner (John Fluke Model 2204A) and pressure scanner (Scanivalve Model J) are controlled and recorded by an on-line, computer-operated data acquisition system.

In measuring the sound intensity to be used as the overall indicator of acoustic level in the test section, we have to take care not to place a microphone at the node of the standing acoustic waves. At higher normal modes, where the spatial separation between nodes becomes narrower, any location of the microphone with its finite size can inevitably infringe upon one of the many nodes. However, the improper installation of it at the node of the fundamental frequency, for instance, would give a falsely lowered level at the lock-in. Therefore, the microphone, which is on the sidewall of the test section, is normally placed at $y = 1.905$ cm (and at $x = 5.08$ cm);

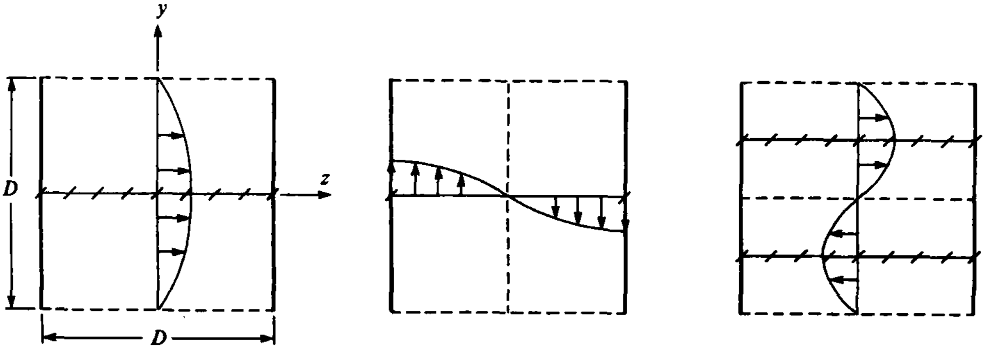

(*a*) $n = 0$, $m = 1$ (*b*) $n = m = 1$ (*c*) $n = 0$, $m = 2$

FIGURE 4. Predicted acoustic modes for v': ⟋⟋⟋ , predicted loop; ----, predicted node.

though it corresponds to the node of the 4th harmonics at the first lock-in, it is found to serve as a satisfactory, general indicator of the sound level of the fundamental, second and third harmonics.

A condenser microphone with a head 0.635 cm in diameter (Bruel and Kjaer Type 4136) is used and its output is fed into FFT high-resolution signal analysers (Bruel and Kjaer Type 2033 for a single channel operation and 2032 for dual channels).

3. Expected acoustic modes at the lock-in

We expect that at the lock-in, where the shedding frequency of a vortex street becomes entrained to that of an acoustic wave, the acoustic modes correspond to the waves standing in the y- and z-directions. Such standing waves, corresponding to a square cross-section of the test section with height D, are given, in the absence of the cylinder, by

$$p' = p_0 e^{i\omega t} \cos\frac{m\pi}{D}(y+\tfrac{1}{2}D)\cos\frac{n\pi}{D}(z+\tfrac{1}{2}D), \tag{1}$$

where p' is the unsteady pressure, m and n are integers and

$$\omega = a_\infty \pi \frac{(n^2+m^2)^{\frac{1}{2}}}{D}. \tag{2}$$

The corresponding unsteady velocity in the vertical y-direction is given by

$$v' = v_0 e^{i\omega t} \sin\frac{m\pi}{D}(y+\tfrac{1}{2}D)\cos\frac{n\pi}{D}(z+\tfrac{1}{2}D). \tag{3}$$

Figure 4, referred to in §1, which shows schematically where the loops and nodes are, corresponds to these normal modes of v'; loops are defined as points possessing the maximum attainable amplitude, v_0, nodes as $v' = 0$. As mentioned, the mode with $n = 0$ and $m = 1$ is expected to correspond to the fundamental frequency of the first lock-in, the mode $n = m = 1$ to the fundamental of the second lock-in and so forth.

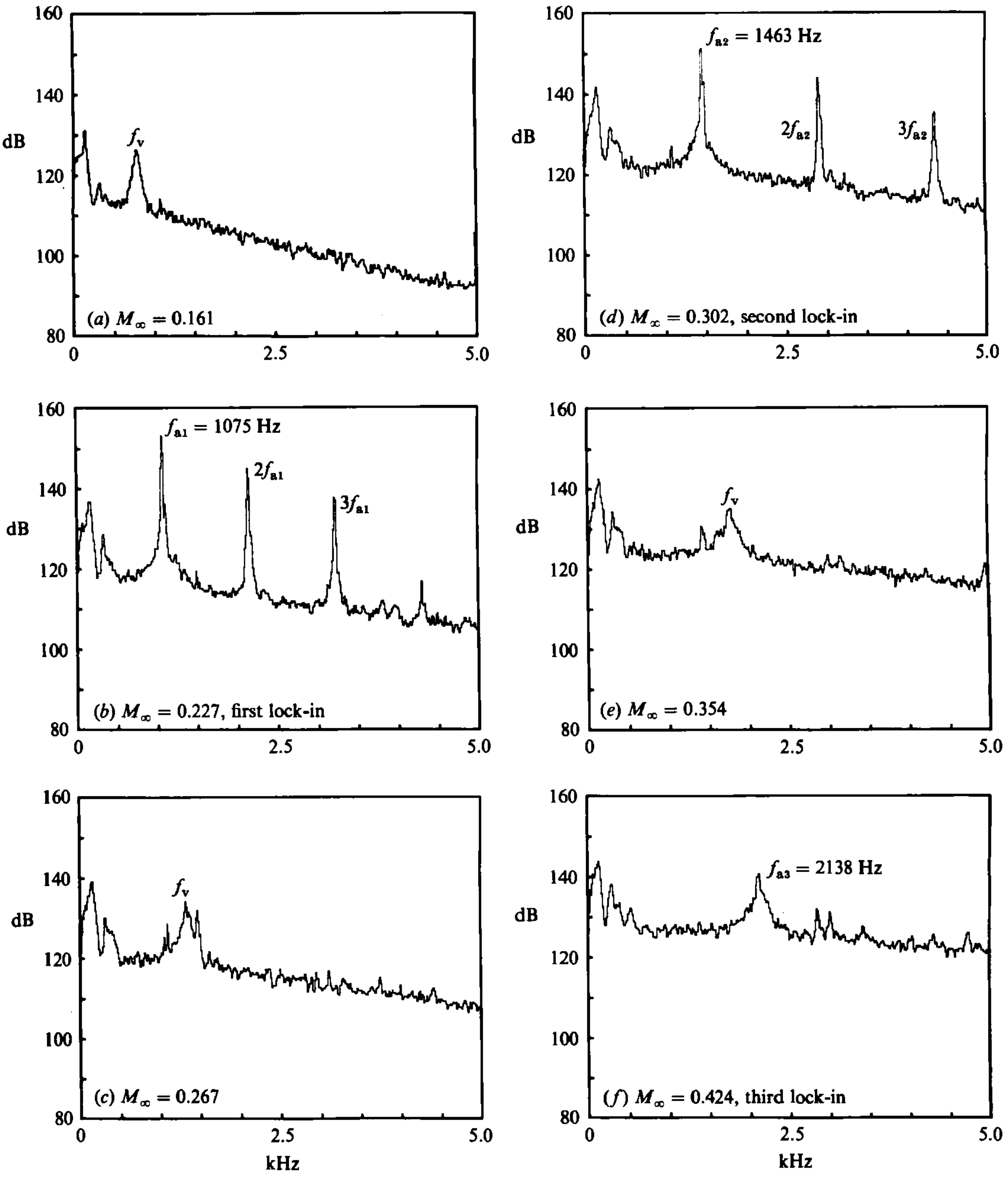

FIGURE 5. Change in spectra.

4. Results for the acoustic enhancement of cooling

4.1. *Acoustic measurements*

Figure 5 (a–f) displays, as the Mach number is progressively increased, the successive change of the frequency spectra obtained by the microphone placed as described in §2. At the low Mach number of 0.161, figure 5 (a), there exists only a single peak f_v, which increases as the Mach number is increased. The peak corresponds to the

Strouhal number of 0.19, a typical value for vortex shedding in the present subcritical Reynolds-number range. As the Mach number approaches 0.206, a ringing sound emerges; for $0.206 < M_\infty < 0.231$, the shedding frequency becomes, as shown in figure 5(*b*), locked to $f_{a1} = 1075$ Hz, which will be confirmed to be the fundamental frequency for the acoustic mode with $n = 0$, $m = 1$. During this first lock-in, in addition to the increasing sound power, higher harmonics appear.

Once past the first lock-in, the sound level falls off sharply and the frequency disengages from the acoustic frequency and resumes its increase with free-stream velocity. The spectrum in figure 5(*c*) reverts to a single peak until the second lock-in, another audible regime, is reached, figure 5(*d*); there the shedding frequency now becomes locked to $f_{a2} = 1463$ Hz, which is found to correspond to the $n = m = 1$ mode, and higher harmonics reappear.

Beyond this, the f_v-frequency disengages from f_{a2} once again (figure 5*e*) until at the third lock-in (figure 5*f*), it becomes locked to $f_{a3} = 2138$ Hz, almost twice that of f_{a1}; the sound level at the third lock-in, however, is not as high as the first and second lock-in and only the peak of the fundamental (f_{a3}) stands out. The reason for this can be inferred from the acoustic waveform shown in figure 4(*c*): there, the node for v' is located on the cylinder axis, the wrong place to elevate a vortex street to higher intensity.

Identification of various acoustic modes corresponding to multitudinous peaks in the frequency spectra at lock-ins can most easily be accomplished by looking at figures 6 and 7: at the first and second lock-in, measured sound levels corresponding to a given peak are shown together with the expected waveform of fluctuating acoustic pressure p', its loops and nodes corresponding to the combination of n and m. To measure the sound intensity the microphone was moved along the periphery of the test section at a cross-section corresponding to $x = 5.08$ cm, 4 diameters downstream of the cylinder. The loop of p' is defined as the location where the amplitude of p' takes its maximum p_0 in (1), and the node at $p' = 0$. Note that while figures 6 and 7 display the waveforms of p', figure 4 shows the waveforms of v'. In addition to the agreement between the measured level for the fundamental and its expected waveform, in figures 6 and 7 we observe that even those for higher harmonics stand similarly favourable comparison.

Besides these, further confirmation of acoustic modes n and m can be established from the comparison of the measured frequency, $f = \omega/2\pi$, with the values calculated from (2). Table 1 shows good agreement between the calculated and measured frequencies. Though, for the reason already stated, at the third lock-in the measured sound level and acoustic loop and node for $n = 0$, $m = 2$ do not agree (figure 8), the frequency calculated for such values of n and m still compares favourably with the data.

In calculating frequency from (2), the propagation of acoustic waves in the streamwise x-direction is neglected. The wavelength in the x-direction λ_x is in fact measured to be larger than that in the y- and z-directions (λ_y and λ_z) from Lissajous figures obtained from two microphones placed at different stations in the x-direction. λ_x for the fundamental at the first lock-in is found to be about 152 cm, in comparison with $\lambda_y = \lambda_z = 30.4$ cm; the influence of λ_x on ω amounts to only 6%.

For a vibrating cylinder, subharmonic or superharmonic resonance is found to occur (Bishop & Hassan 1964; Toebes 1969; Stansby 1976): lock-in takes place not only when the frequency of the vibrating cylinder (f_c) coincides with that of the vortex shedding frequency (f_v) but also when $if_c = jf_v$ (i, j: integers). Although Bearman & Graham (1980) cite the report of Welsh, Parker & Stoneman where such a phenom-

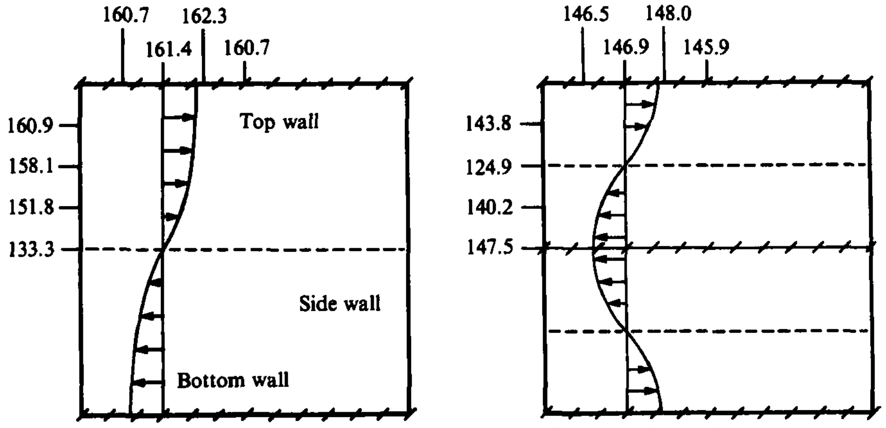

(*a*) Fundamental, $n = 0$, $m = 1$ (*b*) Second harmonics, $n = 0$, $m = 2$

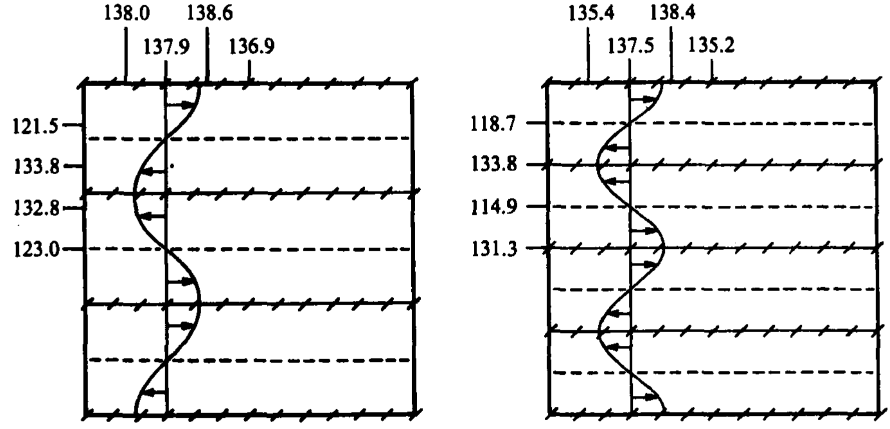

(*c*) Third harmonics, $n = 0$, $m = 3$ (*d*) Fourth harmonics, $n = 0$, $m = 4$

FIGURE 6. Comparison of expected acoustic modes for p' and decibels measured on the wall at the first lock-in, $M_\infty = 0.230$. The numbers denote measured decibels corresponding to (*a*) f_{a1}; (*b*) $2f_{a1}$; (*c*) $3f_{a1}$; (*d*) $4f_{a1}$. -/-/-/- , predicted loop of p'; ----, predicted node of p'.

enon was observed for a flat-plate cascade at acoustic resonance, we did not detect this in our test on a cylinder.

At the present Reynolds number ($Re = 10^5$ at $M_\infty = 0.4$) we also could not detect any peak identifiable at what is commonly referred to as the Bloor frequency (Bloor 1964), a transitional wave observed for the Reynolds number of 10^4; the low-frequency peaks around 125 Hz, common to all the frequency spectra of figure 5, are caused by standing background noise.

For a flat-plate cascade at resonance, Parker (1966) found the existence of what he calls α- or β-modes characterized by the presence of either node (α-mode) or loop (β-mode) at the midchord of the plate; even for a single plate at resonance, the presence of the β-mode was identified by Cumpsty & Whitehead (1971). In the present case of a single cylinder at acoustic resonance no such modes appear to exist.

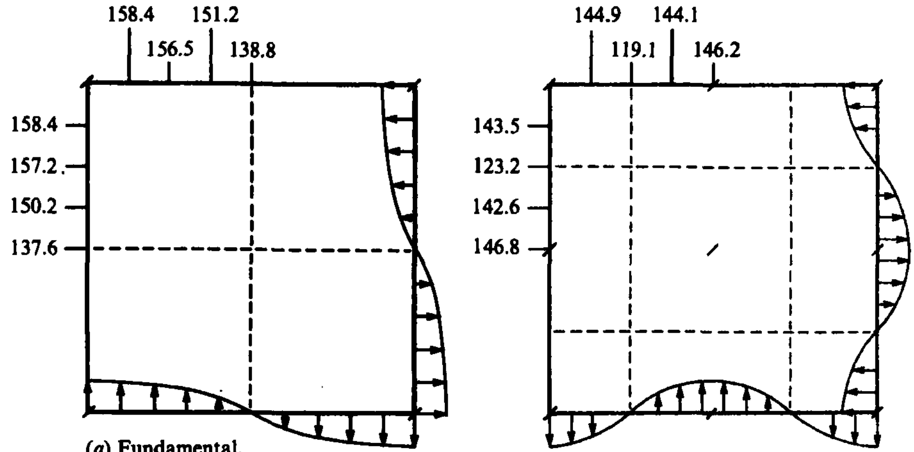

(*a*) Fundamental, $n = m = 1$

(*b*) Second harmonics, $n = m = 2$

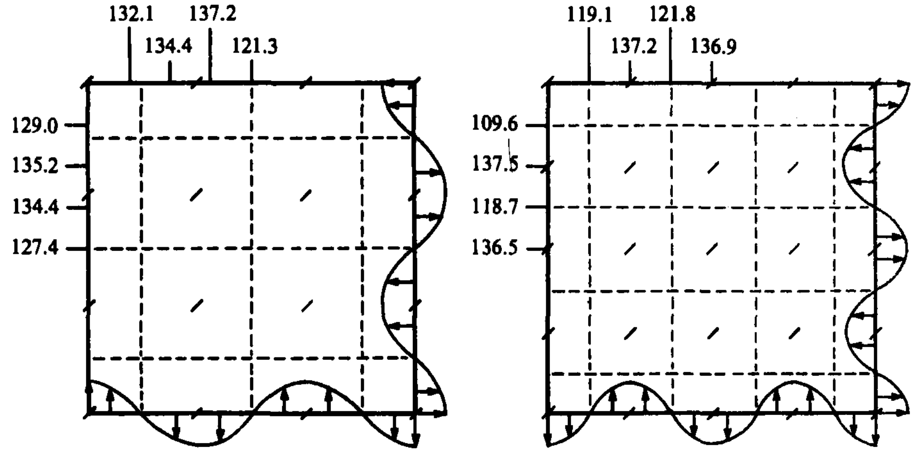

(*c*) Third harmonics, $n = m = 3$

(*d*) Fourth harmonics, $n = m = 4$

FIGURE 7. Comparison of expected acoustic modes for p' and decibels measured on the wall at the second lock-in, $M_\infty = 0.305$. The numbers denote measured decibels corresponding to (*a*) f_{a2}; (*b*) $2f_{a2}$; (*c*) $3f_{a2}$; (*d*) $4f_{a2}$: /, predicted loop of p'; ----, predicted node of p'.

	Acoustic speed calculated from measured temperature (m/s)	Calculated fundamental frequency (Hz)	Measured fundamental frequency (Hz)
(I) first lock-in	338	1109 ($n = 0$, $m = 1$)	1075
(II) second lock-in	333	1544 ($n = m = 1$)	1463
(III) third lock-in	325	2132 ($n = 0$, $m = 2$)	2138

TABLE 1

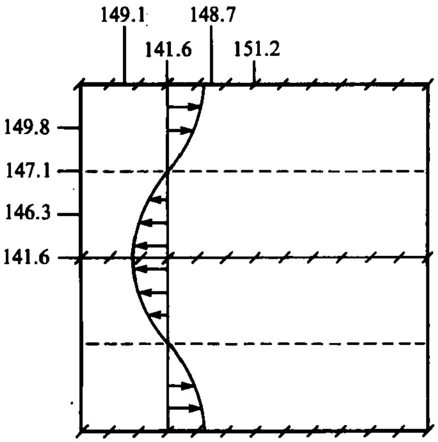

FIGURE 8. Comparison of the expected acoustic mode for $p'(n = 0, m = 2)$ and decibels measured on the wall at the third lock-in, $M_\infty = 0.426$. The numbers denote measured decibels corresponding to f_{a3}; ⫽⫽⫽, predicted loop of p'; ----, predicted node of p'.

4.2. *Surface pressure and temperature at acoustic resonance*

Before examining the correlation of acoustic resonance with surface pressures and temperatures, we first consider figure 9(*a*–*c*), which summarizes the successive change in the acoustic signals described in §4.1; in them, the fundamental frequency, the corresponding Strouhal number and decibels of the fundamental frequency are plotted versus the free-stream Mach number, with I, II and III denoting the aforementioned lock-in regimes.

Our key results are presented in figure 9(*d*), for the base pressure coefficient C_{pb} and figure 9(*e*), for the recovery factor R, both at $\theta = 180°$. Here C_{pb} and R are defined as

$$C_{pb} = \frac{p(\theta = 180°) - p_\infty}{\frac{1}{2}\rho_\infty U_\infty^2},$$

$$R(180°) = \frac{T(\theta = 180°) - T_\infty}{T_{t\infty} - T_\infty},$$

where $p(\theta = 180°)$ and $T(\theta = 180°)$ are the surface pressure and temperature at $\theta = 180°$, respectively, p_∞ the upstream static pressure, ρ_∞ the upstream density, T_∞ the upstream static temperature and $T_{t\infty}$ the upstream total temperature, here taken as the value at $\theta = 0°$, located on the opposite side of the measurement point $\theta = 180°$ (the choice of this as $T_{t\infty}$ rather than in the settling tank is found to reduce the scatter in data; in all tests, C_p at $\theta = 0°$ remained close to unity, as expected). The measurements are taken at the three spanwise stations mentioned above: (1) the midspan point (2) a quarter-span point and (3) a near-wall point. For our present purpose, no corrections to C_{pb} for the wind-tunnel blockage are judged to be necessary and the data presented are uncorrected.

In figure 9(*d*, *e*), we observe that at the first lock-in, I, both C_{pb} and $R(180°)$ take significant *simultaneous plunges* and this occurs *regardless of the spanwise station*, fulfilling our expectation stated in §1. This dip of C_{pb}, or increased suction behind the cylinder, indicates an increase in drag, which in turn implies intensification of the vortex street. This does indeed cause the drop of the recovery factor at $\theta = 180°$, and it is important to note that $R(180°)$ becomes *negative* even at this low subsonic

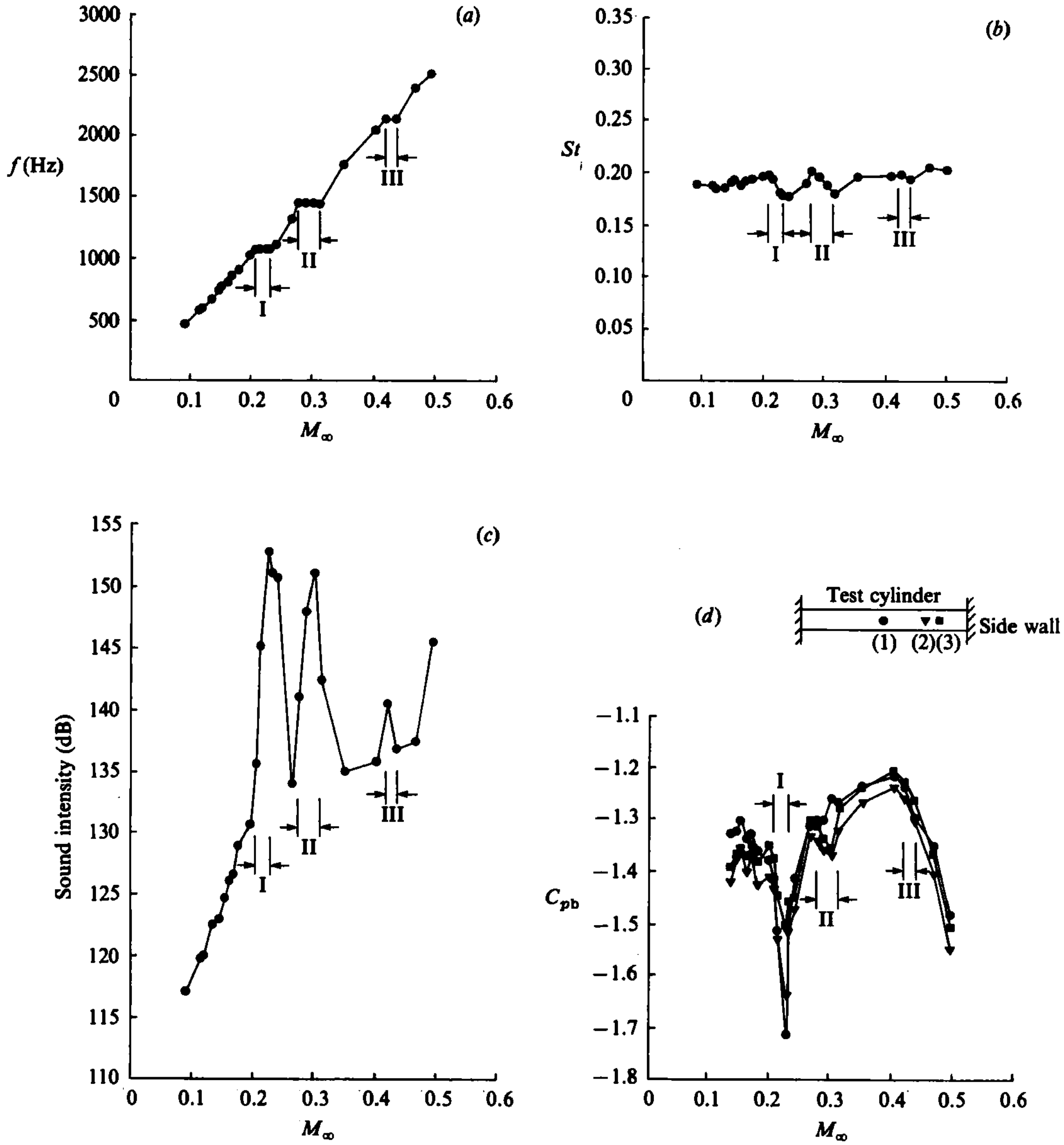

FIGURE 9(*a–d*). For caption see next page.

Mach number of 0.21. The intensified strength of vortices at acoustic resonance may be attributable to the increase of circulation around the cylinder, caused by the shift in the forward stagnation point owing to the presence of fluctuating acoustic velocity. This intensification and the improvement in spanwise correlation is similar to that of a transversely vibrating cylinder (Taneda & Honji 1967; Toebes 1969; Berger & Willie 1972; Griffin & Ramberg 1975).

In contrast to the first lock-in, at the second lock-in II, figure 9(*d*, *e*) shows that dips in C_{pb} and R occur only at stations (2) and (3), points located off the centre, while at the mid-span point (1) no such sharp drop is observed. This also substantiates our expectation stated in §1 – the strength of vortex streets *vary along the span* in response to acoustic nodes and loops.

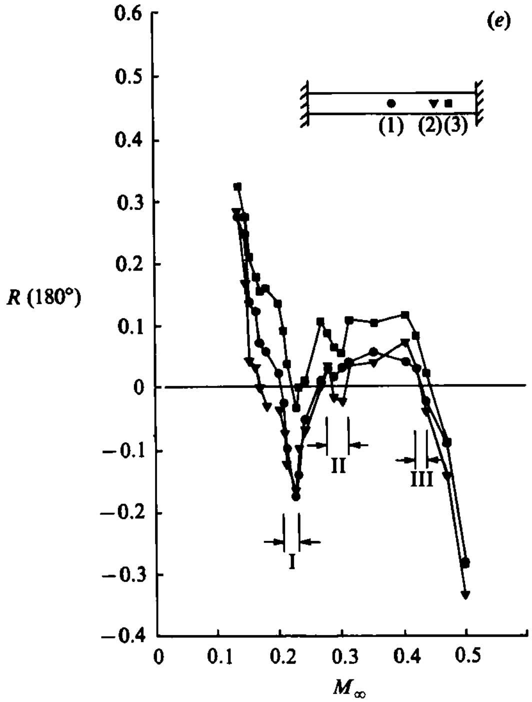

FIGURE 9. Main test results. (*a*) Fundamental frequency versus free-stream Mach number. (*b*) Strouhal number versus free-stream Mach number. (*c*) Sound intensity of fundamental frequency versus free-stream Mach number. (*d*) Base pressure coefficient versus free-stream Mach number. (*e*) Base recovery factor versus free-stream Mach number. For (*d*), (*e*), measurements taken at (1) the midspan point, (2) a quarter-span point, (3) a near-wall point, the direction of the flow being out of the paper.

This behaviour of vortex streets has been previously found in somewhat different circumstances: for a stationary straight cylinder immersed in a shear flow (Chen & Mangione 1969) or for a stationary tapered cone in a uniform flow (Taneda 1965), the vortex-shedding frequency varies along the span in such a way that if one takes either a local velocity or a local diameter, the Strouhal number always remains the same as that for the two-dimensional case, a straight cylinder in a uniform flow. Here the strength of vortex streets is found to vary along the span in such a way that it responds two-dimensionally to *varying* stimuli; in all of these the 'strip theory' apparently holds but in the present case it is demonstrated for the intensity of vortices rather than for the shedding frequency.

From the waveform of figure 4(*b*), which shows 180° phase lag between two loops of v' on the sidewalls, the vortex shedding near both ends of the cylinder at the second lock-in may well be out of phase. Though this point has not been pursued, among the data obtained for flat-plate cascade acoustic resonance (Hiramoto *et al.* 1972), there is supporting evidence showing that the response of vortex shedding for two such loops may indeed be out of phase.

In contrast to the first and second lock-ins, the third lock-in corresponding to the $n = 0$, $m = 2$ acoustic mode exhibits no dips in either $C_{p\mathrm{b}}$ or $R(180°)$; this reflects weaker resonance at the third lock-in, as discussed in §4.1.

As the Mach number is increased further, the Prandtl–Glauert effects come into play, resulting in the general increase of $|C_{p\mathrm{b}}|$ and $|R(180°)|$ even in the absence of resonance. Since the objective of our study is realizing the Eckert–Weise effect or negative recovery factor at resonance in the *low subsonic flow*, the present Mach numbers are less than 0.5. The trend beyond this Mach number may be discerned from the measurements of Thomann (1959), taken in the absence of acoustic resonance: $R(180°)$ attains a minimum at around $M_\infty = 0.65$ and then it starts to increase until it reaches 0.8 at around $M_\infty = 1$. This increase at transonic flow and beyond is almost certainly caused by the narrow-'necked' wake and the resulting weakened vortex strength.

To sum up the experimental results, by establishing in general the correlation between acoustic resonance and its influence upon the recovery factor, our measurements indeed confirm the earlier speculation of Ryan (1951) stated in §1. The results demonstrate in particular (*a*) the attainment of the negative recovery factor even at the low Mach numbers of 0.2 (at the first lock-in), (*b*) its link with the intensification of the vortex street uniformly along the span through the corresponding behaviour in the base pressure, and (*c*) the local correlation between the recovery factor varying along the span and the strength of the vortex street (at the second lock-in). This leaves little doubt that the vortex street is indeed the cause of the Eckert–Weise effect.

5. The mechanism of instantaneous and time-averaged total temperature distribution: dynamical explanation

In §1, in reference to the computer-generated colour graphics we noted that the instantaneous flow fields (figure 10*a, b*, Plate 2) disclose the unexpected segregation of the total temperature into hot and cold spots; the time-averaged cold wake (figure 1*a*) or the Eckert–Weise effect, however, conceals the presence of the hot spots. We now offer a simple dynamical explanation for this instantaneous energy separation by vortices.

Central to the *dynamical* interpretation is the following form of energy equation (e.g. Liepmann & Roshko 1957):

$$c_p \frac{\mathrm{D}T_\mathrm{t}}{\mathrm{D}t} = \frac{1}{\rho}\frac{\partial p}{\partial t}, \tag{4}$$

when T_t is the total temperature, all other notation being standard. Neglect of the dissipation effects will be justified in §6. Here we discuss the consequences of (4) with respect to vortex shedding. Since the left-hand side of (4) involves the variation of total temperature along the particle path or a pathline, before applying the equation, we ought to have a clear grasp of the pathline pattern for a vortex street shed behind a body; although streaklines for a vortex street are observable in many flow visualizations, the *pathlines* are quite different for the present unsteady flow (for a comparison between the two in a vortex street, see Kurosaka & Sundaram 1986).

Consider first pathlines for a single isolated vortex (figure 11). There, any given fluid particle P revolves around the vortex centre O with a rotational velocity u_θ induced by the vortex, while the vortex centre itself is convected in the downstream direction. Let u_v be the convective velocity which is for now taken to be a constant independent of time. At $t = 0$, the vortex centre was passing the y-axis at O' $(0, y_0)$. Then the trajectory of a fluid particle $P(x, y)$ located initially at P' a distance r from the vortex centre, is given, in the laboratory coordinate system, by

$$\left.\begin{aligned} x &= r\left(\frac{u_\mathrm{v}}{u_\theta}\phi + \sin\phi\right), \\ y &= y_0 + r\cos\phi, \end{aligned}\right\} \tag{5}$$

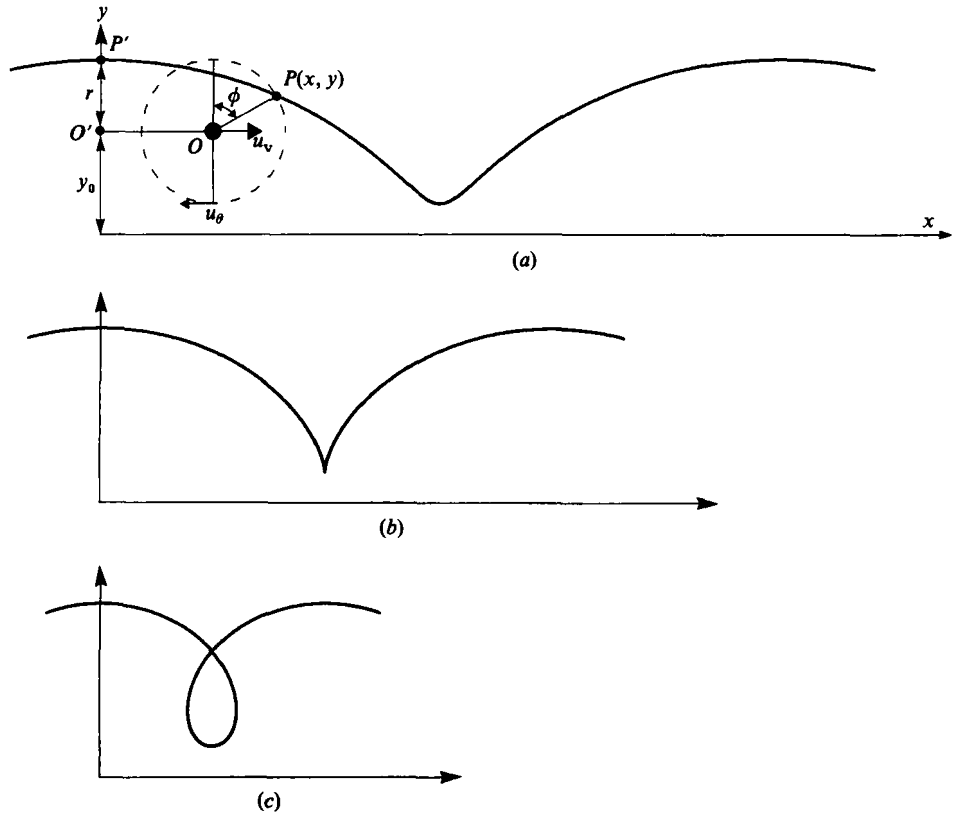

FIGURE 11. Trochoidal pathlines. (*a*) $u_v/u_\theta > 1$ curtate; (*b*) $u_v/u_\theta = 1$ cycloidal; (*c*) $u_v/u_\theta < 1$ prolate.

where $\phi = (u_\theta/r)\,t$. These are parametric equations for trochoids (for photographic evidence for trochoidal pathlines, see figure 14 of Kirde 1962). As shown in figure 11, trochoidal curves take different shapes depending upon whether u_v/u_θ is larger or less than 1: (*a*) curtate for $u_v/u_\theta > 1$, (*b*) cycloidal for $u_v/u_\theta = 1$ and (*c*) prolate for $u_v/u_\theta < 1$. (*a*) and (*c*) are generalization of a cycloid (*b*), which is the trajectory traced out by a fixed point on a wheel rolling along a straight line without slipping.

Even for vortices in a vortex-street arrangement, so long as a fluid particle is initially located in the vicinity of a vortex, the subsequent trajectory remains nearly trochoidal (Kurosaka & Sundaram 1986).

Although pathlines take various trochoidal shapes, the application of (4) to any of these reveals a feature common to all: the separation of T_t around vortices. Take, for instance, a curtate trochoidal type. Figure 12 shows a *single* and the same fluid particle at 3, 6, 9 and 12 o'clock along a curtate trochoidal path, revolving around a vortex centre convected downstream. In applying (4), note one additional point: the pressure falls toward the vortex centre. Therefore, for the fluid particle momentarily occupying the 3 o'clock position, which the vortex centre is approaching, the pressure there is falling off in time, $\partial p/\partial t < 0$ and from (4), $\mathrm{D}T_t/\mathrm{D}t < 0$. Thus, here T_t decreases along the path. On the other hand, at the 9 o'clock position, from which the centre is receding, the pressure is recovering; T_t is increasing. At 6 or 12 o'clock, the pressure neither rises nor falls: $\partial p/\partial t = 0$ and $\mathrm{D}T_t/\mathrm{D}_t = 0$ and at both positions, T_t assumes extreme values. From these arguments, one can conclude that T_t

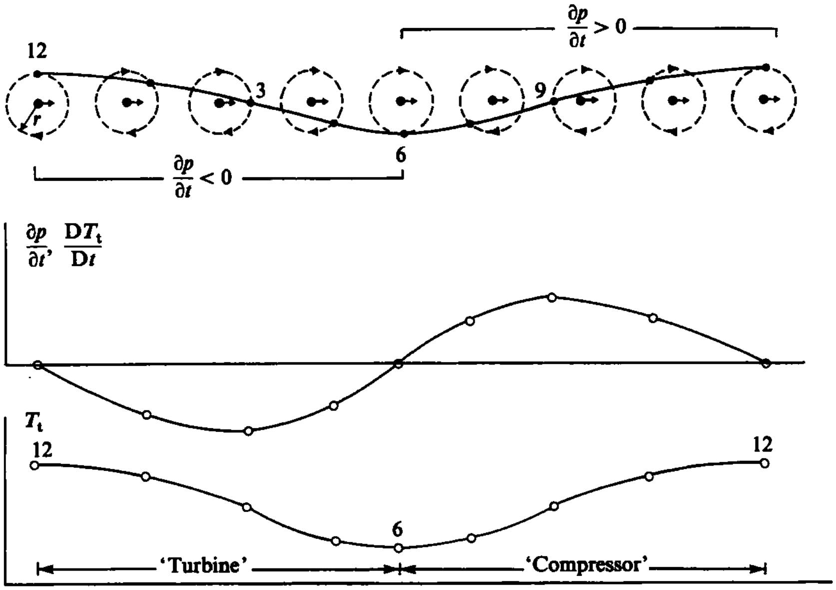

FIGURE 12. Variation of T_t along a curtate trochoidal pathline.

undergoes a cyclic rise and fall, reaching a maximum at 12 o'clock and a minimum at the 6 o'clock position, as shown in figure 12. Around the circumference of a vortex, T_t becomes separated.

Since T_t decreases or increases during each half-cycle, one may call the $12 \rightarrow 3 \rightarrow 6$ half-cycle a 'turbine', $6 \rightarrow 9 \rightarrow 12$ a 'compressor'; two fluid particles, each belonging to 'compressor' and 'turbine' half-cycles, respectively, exchange work.

These results also hold for other trochoidal pathlines, whether cycloidal or prolate. When we apply these arguments, based on a single vortex, to a vortex street, the only difference is that the T_t separation becomes *directionally oriented*; in the vicinity of any vortices, cold spots with lower T_t appear on one side of the wake centreline, hot spots with higher T_t on the other side, the free stream side, and this occurs on account of the clockwise circulation in the upper-row vortices and counterclockwise in the lower ones. The entry of the fluid particle into the vortex street decreases T_t, the exit increases it.

Let us now interpret the colour graphics in the light of these considerations. Compare figure 10(*a*), an instantaneous total temperature distribution, with 10(*c*), the corresponding vorticity distribution, and 10(*b*) with 10(*d*); in vorticity plots the clockwise vorticity is shown by colours at the red end of the spectrum, counterclockwise blue, the incoming irrotational flow yellowish-green (the white spot again corresponds to the region with vorticity a grade or two higher than the maximum pink). Compare patches of vorticity with their corresponding positions in the T_t distributions. Around any intense region of vorticity hot spots exist, as expected, on the free stream side and cold spots on the side of the wake, all with varying degrees of T_t separation. Most conspicuous is that where a vortex is being torn, breaking away from its feeder line adhering to the cylinder. Corresponding to the splitting of an initial vorticity patch into two (figure 10*d*), thermal separation is also observed to separate into two, with two purple–white spots (10*b*).

As stated, successive superposition of instantaneous T_t distributions such as figures

10(*a*) and (*b*) yields the time-averaged T_t distribution, figure 1(*a*) (the corresponding time-averaged vorticity distribution, figure 1(*b*), compares favourably with experimental results, such as figure 21(*a*) of Cantwell & Coles 1983).

6. Additional remarks on the mechanism

It is instructive to offer an alternative explanation of the dynamical process of T_t separation. Consider again the particle moving along the curtate trochoidal pathline of figure 12 and focus attention on the pressure acting on the particle momentarily occupying the 3 o'clock position. When the radial pressure gradient $\partial p/\partial r$, present in the moving-vortex coordinate system and counterbalancing the centrifugal force, is decomposed in directions tangential and normal to the pathline, its tangential component is oriented in the direction opposing the movement of the particle (its normal component is of course balanced by a centrifugal force associated with the curvature of the pathline). Thus the kinetic energy of the fluid particle ($\frac{1}{2}q_t^2$, where q_t is the tangential velocity) decreases owing to the work done by the pressure. On the other hand, the static temperature T, which is dependent[†] only on the radial distance r between the fluid particle and the vortex centre, remains unchanged along the pathline. Hence the total enthalpy or $T_t = T + (1/2c_p)\,q_t^2$ decreases in the half-cycle between 12→3→6 o'clock positions while in the other half it increases.

In addition to a trochoidal pattern, there exists a pathline belonging to a distinctly different class, called here cross-over type. Its shape appears to defy our intuition. As observed in figure 13, the fluid particle starts at the upper half of the flow, traverses the wake centreline and eventually ends in the lower half. The initial downward entrainment in figure 13(*a*) is caused by the slight imbalance between vertical components of velocity, induced by vortices on the fluid particle at a point such as B, located nearly midway between vortices 1 and 3 but on the upstream side. The expulsion from the vortex street (figure 13*b*) is caused by a similar imbalance after the particle reaches the lower row of vortices, approaching C, nearly midway between two adjacent vortices 2 and 4 but on the downstream side. It is not difficult to ascertain this odd-looking pathline by releasing coloured dye on one side of the vortex street shed behind a cylinder in water and witnessing that, when the release is well-timed, it does end up on the other side[‡] (see figure 14, Plate 3; although the pictures show dye lines, not pathlines, the point is that fluid particles do cross the wake). The presence of cross-over as well as trochoidal pathlines, can also be confirmed by the results of numerical simulations of vortex shedding (see figure 9 of Davis & Moore 1982; R. W. Davis, 1985, private communication).

Consider the variation of T_t along a cross-over type pathline. Seen from figure 13(*a*), in its initial phase of entry into the vortex street, the fact that the fluid particle becomes entrained at all implies that the vortex 3 exerts a stronger influence than 1; thus, for the fluid particle at position B, the effect of approaching vortex 3 is similar to that of 3 o'clock position for a trochoidal pathline; T_t falls. The reverse is true for position C. In its course along the cross-over pathline, T_t first undergoes a fall and then a rise, with its lowest value attained at or near the wake centreline.

When we take an average of T_t in the streamwise direction, which is equal to its temporal average, the lowered value of T_t at points such as A tends to cancel the

---

[†] Compared with the explanation given in §5, this assumption on T is the additional constraint needed in this line of argument.

[‡] These cross-over pathlines may be responsible for the curious phenomenon of thermal-gradient reversal downstream of a cylinder placed in a duct, as observed by Minchin (1951).

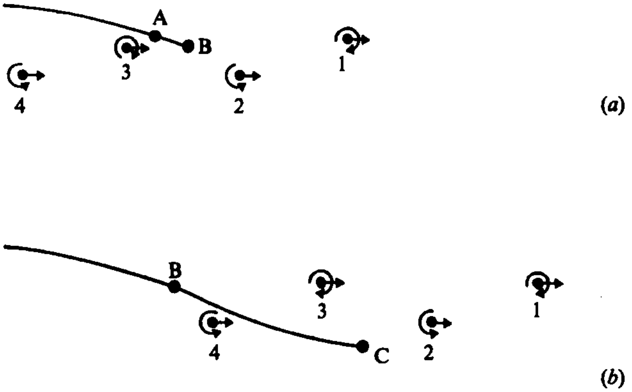

FIGURE 13. Cross-over pathlines. (*a*) Entry of a fluid particle along a cross-over pathline into a vortex street; (*b*) exit.

higher T_t associated with the other fluid particle at the 12 o'clock position along the trochoidal pathline around the vortex 3. This is why the time-averaged T_t distribution can hide the presence of excess T_t.

It is evident from the foregoing argument that the dynamical process of T_t separation does not hinge on the specific details of trochoidal or cross-over pathlines. Both types are brought out to provide graphically illustrative examples; even for all other pathlines, every entry of the fluid particles into the vortex street entails a decrease in T_t and every exit an increase. It is also obvious why the time-averaged T_t should assume its minimum at or around the wake centreline.

In instantaneous T_t distributions, the degree of thermal separation seems to become reduced in the downstream flow field; the defect in time-averaged T_t becomes correspondingly less. Although this may be, to a considerable degree, attributable to the numerical-mesh effect, its physical reason can be explained as follows. We change from the present laboratory coordinates $(x, y; t)$, where the cylinder is stationary, to the vortex coordinate system $(x_v, y_v; \tau)$. When vortices are convected downstream with different speeds, as they do in reality, we move with any one of the vortices, the centre of which is moving with velocity $u_v(t)$ in the x-direction (the movement in the y-direction, though easy to be incorporated, will not be considered here for simplicity):

$$x_v = x - \int_0^t u_v(t)\,\mathrm{d}t, \quad y_v = y, \quad \tau = t. \tag{6}$$

Then (4) becomes

$$c_p \frac{\mathrm{D}T_t}{Dt} = \frac{1}{\rho}\left(\frac{\partial p}{\partial \tau} - u_v(t)\frac{\partial p}{\partial x_v}\right), \tag{7}$$

where $\partial p/\partial \tau$ and $\partial p/\partial x_v$ represent temporal and spatial change in pressure, respectively, both relative to the moving-vortex coordinate. If the vortex were of unchanging strength (an assumption, though unnecessary, tacitly made for the sake of simplicity in the aforementioned pathline argument), then $\partial p/\partial \tau = 0$ and the rate of variation of T_t along pathlines would depend only on the second term, the combined effect of the approach velocity of the vortex centre, $u_v(t)$, and spatial gradient of pressure $\partial p/\partial x_v$; the latter is in turn directly dependent upon the strength of the vortex Γ. In reality, however, in the near wake behind a body, the region of most interest here, the vortex strength does not remain unchanged. For an evolving vortex in paticular, with its strength intensifying with time, the pressure would temporarily decrease even when the vortex did not move: $\partial p/\partial \tau < 0$ (J. E. McCune 1985, private communication). Taken together with the actual movement of the vortex, this leads to the additional lowering of T_{t} at cold spots. This near-wake effect yields a downstream gradient in both instantaneous and time-averaged T_{t} (in the far wake, the gradient is caused by the dissipative effects).

From the foregoing argument, it is obvious that T_{t} around vortices should become separated even when the cylinder is not thermally insulated, although the degree of time-averaged temperature drop is certainly dependent upon the thermal condition on the cylinder surface.

We now discuss why dissipative effects are negligible in the mechanism of instantaneous T_{t} separation. In the place of the approximate equation (4), we write its exact counterpart in the following non-dimensional form:

$$\frac{\mathrm{D}T_{\mathrm{t}}^*}{\mathrm{D}t^*} = \frac{1}{\rho^*}\frac{\partial p^*}{\partial t^*} + \frac{1}{Re}\left(\frac{\tau U_\infty}{d}\right)\left[\Phi^* + \frac{1}{Pr}\nabla^{*2}T^* + \boldsymbol{u}^*\cdot\boldsymbol{F}_f^*\right], \tag{8}$$

where Pr is the Prandtl number, Re the Reynolds number based on the diameter of the cylinder d and starred quantities are all dimensionless; T_{t} and T are non-dimensionalized by U_∞^2/c_p; p by $\rho_\infty U_\infty^2$; ρ by ρ_∞; t by τ, which is a characteristic timescale, the time required for a fluid particle to travel across one full wavelength for a trochoidal pathline or to traverse the wake for a cross-over pathline; Φ, the dissipation function by $\mu U_\infty^2/d^2$; $\boldsymbol{F}_f$, non-dimensionalized by $\mu U_\infty/d^2$, is $\boldsymbol{F}_f = \operatorname{div}[\mu(\operatorname{def}\boldsymbol{u})] + \operatorname{grad}(\lambda \operatorname{div}\boldsymbol{u})$, where def is the deformation tensor, λ the second coefficient of viscosity.

The time-scale τ is of the order of the vortex-shedding period and an estimate yields $\tau U_\infty/d \sim 5$; thus for a flow with a high Reynolds number, the centre of interest, the second term may be discarded. As far as the dynamics of instantaneous change in total temperature is concerned, dissipative effects are then of negligible importance. (However, they of course cumulatively exert a decided effect upon the far downstream T_{t}.)

Equation (4) can therefore be used not only for the qualitative explanation of T_{t} separation, as discussed in the previous section, but also for the *quantitative* calculation of instantaneous T_{t} separation in the near wake, without resorting to the full Navier–Stokes equations. Such a task, though straightforward once we specify a model for the vortex street in the vicinity of the cylinder, is beyond the scope of the present investigation.

7. The dynamical separation of total pressure around vortices

For an incompressible flow, under the same condition for which (4) holds, the internal energy does not vary along pathlines. Then (4) is reduced to

$$\frac{\mathrm{D}P_{\mathrm{t}}}{\mathrm{D}t} = \frac{\partial p}{\partial t}, \tag{9}$$

where P_{t} is the total pressure. Thus the argument previously applied to the separation of total temperature now leads to the similar separation of total pressure for an incompressible flow. For flows at the low Mach number, then, the instantaneous measurements should show that the positions of high T_{t} correspond to high P_{t}, low T_{t} to low P_{t}. In fact, by integrating

$$\rho c_p \frac{\mathrm{D}T_{\mathrm{t}}}{\mathrm{D}t} = \frac{\mathrm{D}P_{\mathrm{t}}}{\mathrm{D}t}, \tag{10}$$

along a pathline starting from far upstream, we obtain

$$\frac{\rho c_p T_{t\infty}}{P_{t\infty}}\left(\frac{T_t}{T_{t\infty}}-1\right)=\frac{P_t}{P_{t\infty}}-1. \tag{11}$$

Thus in the near wake the pattern of the instantaneous distribution of $P_t/P_{t\infty}$ must be an almost exact facsimile of those of $T_t/T_{t\infty}$ (except for a scaling factor of $\rho c_p T_{t\infty}/P_{t\infty}$, which is equal to $\gamma/(\gamma-1)$). This can be directly confirmed by figure 15 (Plate 4), computer-generated colour graphics for $P_t/P_{t\infty}$, and comparing with $T_t/T_{t\infty}$ of figure 10; figure 15(*a*) corresponds to the same-sequence as 10(*a*), 15(*b*) to 10(*b*).

The long-familiar defect in the time-averaged P_t behind a bluff body may thus be subject to the reinterpretation as the superposition of the instantaneous, spatially separated total pressure field in the manner similar to that of the time-averaged Eckert–Weise effect. (Any difference between the time-averaged P_t and T_t should reflect the dissipative effects and is expected to be connected with the entropy rise, a relation to be discussed in §9.)

The data obtained in §4 by acoustic resonance, where the behaviour of base pressure is found to bear a close resemblance to that of the recovery factors, may be construed likewise, since on the body surface P_t and T_t are the same as those of surface pressure and temperature, respectively.

8. Special application to the case of the classical Kármán-vortex-street model: kinematical explanation

The dynamical explanation of the mechanism for the instantaneous T_t separation offered in §5 is obviously not subject to any constraints on the details of the vortex street. It is, for instance, not tied up with any specific idealized model such as the downstream equilibrium configuration of the Kármán vortex street or its variants.

Here, for the sake of completeness and to pave the way for the subsequent discussions of past theories, we consider the model of an infinite vortex street. We show that for such an idealized model a purely kinematical, rather than dynamical, explanation of T_t separation may be deduced and instantaneous T_t distribution can be easily calculated. The drawbacks of the argument, compared to the preceding dynamical explanation, are the need for various restrictive assumptions to be mentioned immediately.

We replace the potential vortices in the classical Kármán vortex street with Rankine vortices, where the viscous cores are approximated by solid rotation. All vortices – circular, axisymmetrical and located equidistantly but alternatingly along two parallel rows – are assumed to be of the same strength and to move with the same celerity; viewed from a coordinate system moving with the vortices, the flow appears to be absolutely steady. It must be said, however, that this model, though somewhat more realistic than the one with potential vortices, is not a close representation of actual vortices, particularly in the near field, the centre of our interest. Chief among the relevant discrepancies with experimental results are the fact that (i) vortices *evolve and diffuse, their celerity does change in the x-direction* (Cantwell & Coles 1983), (ii) observed vortices are *non-circular* (Davies 1976), (iii) even when we choose to ignore the above, then in the coordinate system moving with a vortex we observe that from the cylinder, which now seems to move upstream, vortices appear one by one; thus *even in the vortex coordinates, the flow is never steady.*

Despite this, we consider the T_t distribution in such an infinite vortex street. First it is convenient to express T_t in two coordinate systems: one (denoted by subscript 1) is taken to be the laboratory coordinate, where the cylinder is stationary with free stream velocity equal to U_∞ and all vortices with circulation Γ move downstream with speed u_{v}; second (denoted by subscript 2), the vortex coordinate, where vortices appear steady. Then at any point in the flow, $u_2 = u_1 - u_{\mathrm{v}}$ and $v_2 = v_1$, where v is the transverse fluid velocity. From

$$c_p T_{\mathrm{t}1} = c_p T + \tfrac{1}{2}(u_1^2 + v_1^2), \tag{12}$$

$$c_p T_{\mathrm{t}2} = c_p T + \tfrac{1}{2}(u_2^2 + v_2^2), \tag{13}$$

we obtain

$$c_p T_{\mathrm{t}1} - u_1 u_{\mathrm{v}} = c_p T_{\mathrm{t}2} - \tfrac{1}{2}u_{\mathrm{v}}^2. \tag{14}$$

The left-hand side of (14) corresponds to what is sometimes called, in the terminology of turbomachines where the moving coordinate is rotating, the total rothalpy (Wu 1953).

From (14), it follows that

$$c_p(T_{\mathrm{t}1} - T_{\mathrm{t}1\infty}) = -u_{\mathrm{v}}(U_\infty - u_1) - c_p(T_{\mathrm{t}2} - T_{\mathrm{t}2\infty}). \tag{15}$$

Since the flow viewed from the vortex coordinate is assumed to be steady, then outside of the cores, where to the present order of approximations the flow may be regarded as inviscid, isentropic and irrotational, the total temperature $T_{\mathrm{t}2}$ is uniform; hence

$$c_p(T_{\mathrm{t}1} - T_{\mathrm{t}1\infty}) = -u_{\mathrm{v}}(U_\infty - u_1). \tag{16}$$

Near a given vortex, u_1 is the sum of u_{v} and the streamwise component of the rotational velocity induced by that vortex, u_θ; this leads to a kinematical separation of $T_{\mathrm{t}1}$ around the vortex.

Within cores, we assume that the tangential velocity distribution in the vortex coordinate is, as mentioned, of a solid-rotation type and the static temperature uniform, equal to its value just outside the core. This leads to the following T_{t} separation within cores of vortices:

$$c_p(T_{\mathrm{t}1} - T_{\mathrm{t}1\infty}) = \pm\frac{\Gamma \zeta u_{\mathrm{v}}}{2\pi r_0^2} + u_{\mathrm{v}}^2 - U_\infty u_{\mathrm{v}} - \frac{1}{2}\left[\left(\frac{\Gamma}{2\pi r_0}\right)^2 - \left(\frac{\Gamma r}{2\pi r_0^2}\right)^2\right], \tag{17}$$

where r_0 is the core radius, r the radial distance from the vortex center, ζ the vertical distance from it, and $\pm$ corresponds to vortices belonging to upper and lower rows, respectively. For points at the same radial distance r, the kinematical separation of T_{t} between the upper half of the core ($\zeta > 0$) and the lower half ($\zeta < 0$) is also obvious. Although we have not found any data for core size at high Reynolds number, at low Reynolds number it is known that the core occupies a substantial portion of the wake; for instance, for $Re = 150$, the typical value is $r_0/h \sim 1$, where h is the lateral distance between the two rows of the vortex street (Schaefer & Eskinazi 1959; Griffin & Ramberg 1974).

Figure 16 exemplifies such a calculated, instantaneous distribution of T_{t} throughout the entire vortex street (16*a*), together with the corresponding vortex pattern (16*b*); the latter is viewed from the vortex coordinate rather than the laboratory coordinate in order to enhance the vortical nature of the flow; because of lack of data, r_0/h is assumed to be 0.50 (for these and other details, see Gertz 1985). Figure 17 shows the time-averaged T_{t} distribution, confirming the presence of the coldest spot at the wake centreline, also mentioned previously.

Where the averaged T_{t} at the centreline is concerned, one can evaluate it in an

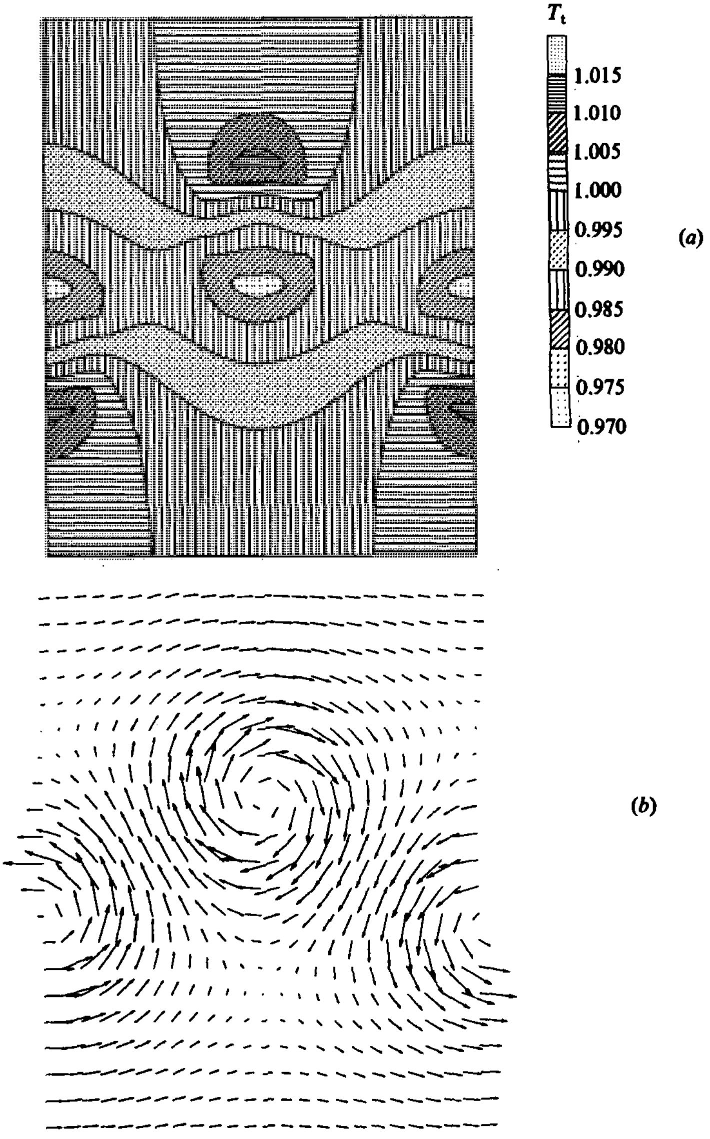

FIGURE 16. Calculated (*a*) T_t distribution and (*b*) vortex pattern for a modified Kármán vortex street. T_t is normalized by $T_{t\infty}$: $M_\infty = 0.35$, $r_0/h = 0.50$, $h/a = 0.281$ (*a*, lateral distance between vortices in the same row), $\Gamma/2\pi a U_\infty = 0.0628$.

explicit form. Take the time-average of (16) and make use of the result (e.g. Lamb 1932) that, for the classical Kármán vortex street, at the centreline of the wake

$$\langle u_1 \rangle = U_\infty - \frac{\Gamma}{a},$$

where Γ is the vortex strength and a the spacing between two adjacent vortices belonging to the same row. Then

$$c_p \langle T_{t1} - T_{t1\infty} \rangle = -u_v \frac{\Gamma}{a}, \tag{18}$$

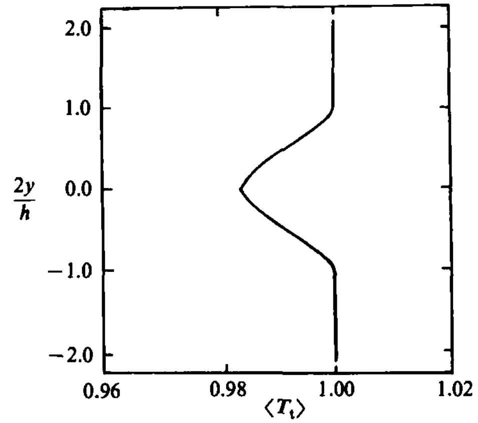

FIGURE 17. Calculated $\langle T_t \rangle$ distribution corresponding to figure 16: y, lateral distance measured from the wake centreline, h, lateral distance between two rows of the vortex street.

at the centreline of the wake. Earlier in this investigation, E. M. Greitzer (1985, private communication) pointed out to us that one can obtain (18) directly by applying the Euler turbine equation, wherein one only has to identify the wheel speed as u_v and connect the difference in the tangential velocity of flow to Γ. The agreement between results based on the two methods is not surprising when one recalls that one way to obtain the Euler turbine equation is to require that the total rothalpy in the rotating coordinate remains the same.

It is fitting at this point to compare the preceding results derived for a specially idealized model with those of previous investigations. Equation (18) is identical with that obtained by Ackeret (1954) under the assumption of an irrotational, potential wake; (16), also valid outside of the core, is, when applied to a single isolated vortex, the same as that of Thomann (1959); incompressible versions, expressed in terms of total pressure rather than the total temperature were obtained independently by Preston (1961). Their kinematical results were all obtained by evaluating $\partial\phi/\partial t$ (ϕ: velocity potential) in the generalized Bernoulli equation, where the flow at the far field is taken to be steady.

The use of the velocity potential ϕ raised an objection from Schlutz-Grunow (1960): he asserted that Ackeret and Thomann had failed to provide proper branch cuts at all vortices in the physical z-plane. So, he rejected out of hand the pioneer results of Ackeret and Thomann, including the prospect of separation of instantaneous total temperature outside of the core, as an outcome of mathematical oversight. This is an unfortunate side issue, and a fallacious one at that, because not only does a constant associated with any branch-cut obviously not matter for $\partial\phi/\partial t$ in an instantaneous flow field, but even for the time-averaged value, branch cuts in the z-plane can be shown to be unnecessary by considering, for instance, a single row of moving vortices†.

The flawed criticism of Schultz-Grunow aside, if we were given only the potential-flow treatment or kinematical argument with its all-too-narrow range of applicability, one might be left uncertain about either the reality or the global validity of the prediction on the unsteady change in T_t. The present paper attempts to emphasize the dynamical argument of the preceding sections, which is unfettered from irksome constraints or unrealistic assumptions, (*a*) by explaining why the instantaneous

† What is needed is a branch cut in the ζ-plane in the complex velocity potential $w = (i\Gamma/2\pi)\log\zeta$, where $\zeta = \sin(\pi(z-u_v t)/a)$, rather than the ones in the z-plane.

separation of total temperature and pressure should occur even in the important near-wake region not representable by the infinite Kármán vortex street, (*b*) by offering evidence that it does occur, and (*c*) by discussing that once it occurs, the separation is not limited to the outside of the core but all portions of the vortex in its entirety becomes separated.

Also concerning past investigations, we should point out that Liepmann & Roshko (1957) turned to (4) as a potential explanation of such problems as the present one and the Ranque–Hilsch effect (in both cases a total temperature change occurs along pathlines). However, their reference was merely made to touch on the general importance of $\partial p/\partial t$ term in an unsteady problem, without going into the explicit and detailed process associated with the vortex dynamics and instantaneous T_t separation (on the temperature separation in the Ranque–Hilsch tube, recent results of one of the authors (Kurosaka 1982), where the mechanism was traced to streaming induced by the vortex whistle, showed that, in addition to the unsteadiness caused by the vortex whistle, the effect of viscosity near the tube wall is important as well).

9. The relationship between the defect in T_t, entropy and drag

The defect in the time-averaged total temperature is, in general, connected with the entropy rise and the cylinder drag.

Consider first the defect in the total pressures P_t between the control surface 1 and 2; control surface 1 is placed far upstream, surface 2 downstream of the cylinder but not necessarily far from it. Then

$$\int_1 P_{t\infty}\,\mathrm{d}y-\int_2 P_t\,\mathrm{d}y=\int_{-\infty}^{\infty}[P_{t\infty}-(P_t)_2]\,\mathrm{d}y=-\int_{-\infty}^{\infty}\mathrm{d}y\int_{-\infty}^{y}\frac{\partial P_t}{\partial y}\,\mathrm{d}y, \tag{19}$$

when $\partial P_t/\partial y$ is to be evaluated on control surface 2. Now from

$$\frac{1}{\rho}\,\delta p+\delta(\tfrac{1}{2}q^2)=c_p\,\delta T_t-T\delta S, \tag{20}$$

where S is the entropy, it follows for incompressible flow that

$$\frac{1}{\rho}\,\delta P_t=c_p\,\delta T_t-T\delta S. \tag{21}$$

When dissipative effects are to be neglected, as in the case of the unsteady separation in T_t and P_t, (21) is reduced to $(1/\rho)\,\delta P_t=c_p\,\delta T_t$, the relationship used in obtaining (9) from (4); here since we are eventually interested in the time-averaged flow including that at downstream points, entropy change is to be retained instead. Substituting (21) into (19):

$$\int_1 P_{t\infty}\,\mathrm{d}y-\int_2 P_t\,\mathrm{d}y=\rho c_p\left[\int_1 T_{t\infty}\,\mathrm{d}y-\int_2 T_t\,\mathrm{d}y\right]+\rho\int_{-\infty}^{\infty}\mathrm{d}y\int_{-\infty}^{y}T\frac{\partial S}{\partial y}\,\mathrm{d}y. \tag{22}$$

As it stands, (22) is applicable at any time. Take the time-average of (22), to be denoted by $\langle\ \rangle$ and then replace T in the second term on the right-hand side with T_∞, an approximation which introduces a second-order error in the term. Then

$$\begin{aligned}&\int_1 \langle P_{t\infty}\rangle\,\mathrm{d}y-\int_2 \langle P_t\rangle\,\mathrm{d}y\\&\quad=\rho c_p\left[\int_1 \langle T_{t\infty}\rangle\,\mathrm{d}y-\int_2 \langle T_t\rangle\,\mathrm{d}y\right]+\rho T_\infty\left[\int_2 \langle S\rangle\,\mathrm{d}y-\int_1 \langle S_\infty\rangle\,\mathrm{d}y\right].\end{aligned} \tag{23}$$

The left-hand side of (23), the defect in total pressure, is now denoted by D'':

$$D'' = \int_1 \langle P_{\mathrm{t}\infty} \rangle \,\mathrm{d}y - \int_2 \langle P_\mathrm{t} \rangle \,\mathrm{d}y. \tag{24}$$

This is related to the (total) cylinder drag D by

$$D'' = D - D', \tag{25}$$

where D' is identical with that adopted by Goldstein (1965) and Saffman & Schatzmann (1982), defined as

$$D' = -\int_2 \rho \tfrac{1}{2}(u'^2 - v'^2)\,\mathrm{d}y, \tag{26}$$

where $u' = u - U_\infty$, $v' = v$. From (23) and (24),

$$c_p\left[\int_1 \langle T_{\mathrm{t}\infty} \rangle \,\mathrm{d}y - \int_2 \langle T_\mathrm{t} \rangle \,\mathrm{d}y\right] = \frac{D''}{\rho} - T_\infty\left[\int_2 \langle S \rangle \,\mathrm{d}y - \int_1 \langle S_\infty \rangle \,\mathrm{d}y\right], \tag{27}$$

which is the desired relationship: the averaged defect in total temperature, multiplied by c_p is equal to the difference between that part of the drag related to total pressure divided by density and the entropy rise times T_∞. Unless the right-hand side becomes zero by an accidental cancellation between two terms, the averaged defect in T_t remains. Except for the assumption of an incompressible flow, (27) is general. We emphasize that the left-hand side is concerned with T_t itself and not with its flux, the latter being, of course, conserved for the present case of a high Reynolds number and a thermally insulated cylinder.

10. Numerical scheme employed in producing colour graphics

We used the explicit, time-marching, unsplit predictor–corrector finite-difference method of MacCormack (1969) as implemented by Shang (1982) to solve the time-dependent, compressible and laminar Navier–Stokes equations for flow past an infinite cylinder. Although the Reynolds number of interest lies in the subcritical régimé and thus the boundary-layer separation is laminar, the transition to turbulence does take place in the wake. However, in the spirit of large-scale structure simulation where the organized vortex dominates the small-scale turbulence – and since we are concerned only with the gross features of vortex shedding – the turbulence model is not implemented. Although this absence of turbulent mixing tends to overpredict T_t separation, particularly in the time-average, the method still evinces qualitatively correct features, which are what we require from the use of computational techniques.

The equations are integrated in time to obtain a 'steady-state' solution from some arbitrary initial state subject to boundary conditions. The method is second-order accurate throughout, but is conditionally stable subject to a Courant–Friedrichs–Lewy time-step restriction. Since details are available in Shang (1982), here we only give a brief outline.

We use a body-oriented coordinate system to transform the polar coordinate in the physical plane into a unit computational square in the transformed space (ξ, η). A uniform grid spacing in the computational space allows a simple implementation of the required finite-difference relationships. The pre-image of this mapping is a highly non-uniform grid in the physical plane, designed to resolve significant flow-field features. The governing equations for mass, momentum and energy are put in conservative form in this (ξ, η) coordinate.

On boundary conditions, the only one differing from Shang is that of the present thermally insulated condition on the wall: $\partial T/\partial r = 0$ on the wall instead of $T = T_w$, the wall temperature.

As described by Shang (1982), the numerical results reproduce, in the course of time marching, the evolution from symmetrically formed twin vortices standing behind the cylinder to the final periodic shedding of alternate vortices; at this final 'steady-state', the stage of our interest, the patterns of instantaneous velocity distribution, the variation of C_p on the cylinder surface, the time-averaged velocity field as well as the Strouhal number are found to compare favourably with available experimental data.

Colour graphics presented in this paper are generated using an AED-512 raster monitor connected to a Matrix Instruments film recorder. The resolution of the device allows a screen of approximately 250000 'pixels' to be defined individually by interpolating a colour value from a table of 250 simultaneously displayable colours arranged in a spectrum according to a range of a dependent variable. Hence, each individual pixel represents a location in the physical grid where we interpolate between the four endpoints of the appropriate grid cell to arrive at a value for the dependent variable (Z) at that location. For each of the plots, the colours range through dark blue (low Z), green, yellow, orange, red, finally to white (high Z).

11. Concluding remarks

In summary, drawing upon a combination of the experimental, theoretical and computational methods, we have investigated the cause and mechanism of the Eckert–Weise effect. By acoustic resonance we first established experimentally that the vortex street is indeed the cause. Through the theoretical and computational investigations, the dynamical mechanism for the instantaneous T_t separation around vortices, which is the root of the effect but hidden in the time-average, is considered. The mechanism comprises three key ingredients: (i) the low-pressure fields at the vortex centres, (ii) their convective movement, and (iii) the entrainment of fluid particles by vortices into the wake and their ejection out of it. The unsteady change in T_t as encountered by a fluid particle along its path may duly be regarded as a natural compressor-turbine process (for an interesting interpretation of the T_t change in turbomachines viewed solely from the unsteady equation (4), see Dean 1959).

For a low subsonic Mach number, P_t is predicted to become separated in a manner similar to T_t. Thus the well-known defect of the time-averaged P_t behind a bluff body may be re-interpreted as the superposition of unsteadily separated structures.

The preliminary results of the time-accurate measurements for T_t and P_t, obtained recently by Chakroun, Ng & Kurosaka (1987) through the use of an aspiration probe, appear to confirm the spatial separation of, and the correlation between, T_t and P_t; it is hoped that the results, once completed, will be published as a sequel to this paper.

The instantaneous T_t and P_t separation, not limited to the vortex street, should be present even in such three-dimensional vortical flows as the large-scale structure along the periphery of jets. The data obtained by Goldstein, Behbahani & Heppelman (1986), which reveals an intriguing anomalous distribution of wall temperatures in the vicinity of an impinging jet, may just be such a manifestation of the effect.

The authors are indebted to the following people at MIT: Professor E. M. Greitzer for all the help and encouragement he has given to us during the course of study; Professor J. L. Kerrebrock for many stimulating discussions, particularly his suggestions related to the alternative explanation in §6; Professor J. E. McCune for his insistence on the importance of inviscid process for the problem in hand and of pathlines; Dr C. S. Tan for helpful comments. Thanks are also due to Dr R. W. Davis of the National Bureau of Standards for sharing generously with us additional pathline calculations and to referees for providing valuable comments on the original manuscript. The authors also wish to acknowledge the suggestion made by Professor R. L. Young of UTSI to use an evacuated cylinder and thank Professors E. E. Covert, E. R. G. Eckert, A. H. Epstein and F. E. Marble and Dr J. S. Shang for their interest and encouragement. The investigation is supported in part by the Air Force Office of Scientific Research under Grant No. AFOSR-83-0049. That part of the work of M. K., carried out during his stay at MIT, was also supported by the grant and in part by the Turbomachinery Research Fund from the General Electric Company to MIT Gas Turbine Laboratory.

REFERENCES

Ackeret, J. 1954 *Mitteilungen aus dem Institute für Aerodynamik* No. 21. ETH, Zürich.

Bearman, P. W. & Graham, J. M. R. 1980 *J. Fluid Mech.* **99**, 225–245.

Berger, E. & Willie, R. 1972 *Ann. Rev. Fluid Mech.* **4**, 313–340.

Bishop, R. E. D. & Hassan, A. Y. 1964 *Proc. R. Soc. Lond.* **A277**, 51–75.

Bloor, M. S. 1964 *J. Fluid Mech.* **19**, 290–304.

Cantwell, B. & Coles, D. 1983 *J. Fluid Mech.* **136**, 321–374.

Chakroun, W. M., Ng, W. F. & Kurosaka, M. 1987 *Ann. Tech. Rep.* (1986) *for AFOSR-83-0049.* U.S. Air Force Office of Scientific Research.

Chen, C. F. & Mangione, B. J. 1969 *AIAA J.* **7**, 1211–1212.

Cumpsty, N. A. & Whitehead, D. S. 1971 *J. Sound Vib.* **18**, 353–369.

Davies, M. E. 1976 *J. Fluid Mech.* **75**, 209–231.

Davis, R. W. & Moore, E. F. 1982 *J. Fluid Mech.* **116**, 475–506.

Dean, R. C. 1959 *Trans. ASME* **81**, 24–28.

Eckert, E. R. G. 1984 *Mech. Engng* **106**, 58–65.

Eckert, E. R. G. & Weise, W. 1943 *Forschg. Ing. Wesen.* **13**, 246–254.

Gertz, J. B. 1985 Unsteady design-point flow phenomena in transonic compressors. Ph.D. thesis, MIT.

Goldstein, S. (ed.) 1965 *Modern Developments in Fluid Dynamics*, vol. II, p. 561. Dover.

Goldstein, R. J., Behbahani, A. I. & Heppelman, K. K. 1986 *Intl J. Heat Mass Transfer* **29**, 1227–1235.

Griffin, O. M. & Ramberg, S. E. 1974 *J. Fluid Mech.* **66**, 553–576.

Griffin, O. M. & Ramberg, S. E. 1975 *J. Fluid Mech.* **69**, 721–728.

Hiramoto, M., Kaji, S., Okazaki, T. & Kishimoto, K. 1972 *Trans. JSME* **38**, 1353–1361 (in Japanese).

Kirde, K. 1962 *Ing. Arch.* **31**, 385–404.

Kurosaka, M. 1982 *J. Fluid Mech.* **124**, 139–172.

Kurosaka, M. & Sundaram, P. 1986 *Phys. Fluids* **29**, 3474–3477.

Lamb, H. 1932 *Hydrodynamics*, 6th edn, p. 225. Dover.

Liepmann, H. W. & Roshko, A. 1957 *Elements of Gas Dynamics*, p. 190. Wiley.

MacCormack, R. W. 1969 *AIAA Paper* 69–354.

Minchin, L. T. 1951 In *Proc. of the General Discussion on Heat Transfer, Sept. 1951*, p. 485. The Institution of Mechanical Engineers and the American Society of Mechanical Engineers.

Parker, R. 1966 *J. Sound Vib.* **4**, 62–72.

Preston, J. H. 1961 *Aero. Quart.* **12**, 343–360.

Roshko, A. 1955 *J. Aero. Sci.* **22**, 124–132.

RYAN, L. F. 1951 Experiments in aerodynamic cooling. Ph.D. thesis, ETH, Zürich.

SAFFMAN, P. G. & SCHATZMANN, J. C. 1982 *J. Fluid Mech.* **122**, 467–486.

SCHAEFER, J. W. & ESKINAZI, S. 1959 *J. Fluid Mech.* **6**, 241–260.

SCHULTZ-GRUNOW, F. 1960 Theory and Fundamental Research in Heat Transfer. In *Proc. the Annual Meeting of ASME* (ed. J. A. Clark), pp. 87–103. Pergamon.

SHANG, J. S. 1982 *AIAA Paper* 82-0098.

STANSBY, P. K. 1976 *J. Fluid Mech.* **74**, 641–665.

TANEDA, S. 1965 *J. Phys. Soc. Japan* **20**, 1714–1721.

TANEDA, S. & HONJI, H. 1967 *Rep. Res. Inst. for Appl. Mech.*, vol. 15, No. 50, pp. 83–92.

THOMANN, H. 1959 *FFA Report 84*. Stockholm.

TOEBES, G. H. 1969 *Trans. ASME* D. *J. Basic Engng* **91**, 493–505.

WU, C. H. 1953 *Trans. ASME* **75**, 802.